



Article

Towards an Integrated Observational System to Investigate Sediment Transport in the Tidal Inlets of the Lagoon of Venice

Gian Marco Scarpa ¹, Federica Braga ^{1,*}, Giorgia Manfè ¹, Giuliano Lorenzetti ¹ and Luca Zaggia ²

¹ Institute of Marine Sciences-National Research Council (CNR-ISMAR), Castello 2737/F, 30122 Venice, Italy; gianmarco.scarpa@ve.ismar.cnr.it (G.M.S.); giorgia.manfe@ve.ismar.cnr.it (G.M.); giuliano.lorenzetti@ve.ismar.cnr.it (G.L.)

² Institute of Geosciences and Earth Resources-National Research Council (CNR-IGG), Via Gradenigo, 6, 35131 Padova, Italy; luca.zaggia@igg.cnr.it

* Correspondence: federica.braga@ismar.cnr.it

Abstract: An observation system integrating satellite images, in situ water parameters and hydrodynamic measurements was implemented in a tidal inlet of the Venice Lagoon (Northern Adriatic Sea, Italy). The experimental infrastructure was developed to autonomously investigate suspended sediment dynamics in the two channels of the Lido inlet in relation to the longshore currents in the littoral zone and the tidal circulation along the lagoon channel network. It provided time series of turbidity at the surface, water flow and acoustic backscatter, which was converted into turbidity along the vertical column during different tidal phases and meteo-marine conditions. Accurate turbidity maps were derived from Sentinel-2 (Copernicus) and Landsat 8 (NASA) satellites. Long-term in situ data from field surveys enabled the calibration and intercalibration of the instrumental setup and validation of satellite-derived products. Time series from the instrumental network were analyzed in order to evaluate the temporal variability of suspended sediment in relation to tidal phases and the different meteo-marine conditions. The integration of available datasets with satellite images also permitted the testing of the methodology for a 3-D reconstruction of the suspended sediment pattern in calm sea conditions, under the effect of the sole hydrodynamical forcing. Remotely sensed data provide a synoptic distribution of turbidity in the inlet area allowing the analysis of the surficial patterns of suspended sediment and the inferring of information on the transport processes at different spatial scales. In calm sea conditions, the results show that the transport is driven by tidal currents with a net seaward transport related to a larger export of materials from the northern basin of the Lagoon of Venice. During typical northeasterly storms, materials mobilized on the beaches and in the shoreface are transported into the inlet and distributed into the lagoon channel network, following the flood tidal currents and determining net import of materials. The multitude of information provided by this system can support research on aquatic science (i.e., numerical simulations) and address end-user community practices. The ecosystem management will also benefit operational purposes, such as the monitoring of morphological transformations, erosion processes and planning of coastal defense in the future scenarios of sea level rise. The developed approach will also help to understand how the regulation of the inlet flow introduced by the operation of the flood barriers will affect the fluxes of particles and, in the long term, the lagoon morphodynamics.

Keywords: remote sensing; sediment transport; turbidity; tidal inlets



Citation: Scarpa, G.M.; Braga, F.; Manfè, G.; Lorenzetti, G.; Zaggia, L. Towards an Integrated Observational System to Investigate Sediment Transport in the Tidal Inlets of the Lagoon of Venice. *Remote Sens.* **2022**, *14*, 3371. <https://doi.org/10.3390/rs14143371>

Academic Editors: Michele Innangi and Sara Innangi

Received: 6 May 2022

Accepted: 11 July 2022

Published: 13 July 2022

Publisher's Note: MDPI stays neutral with regard to jurisdictional claims in published maps and institutional affiliations.



Copyright: © 2022 by the authors. Licensee MDPI, Basel, Switzerland. This article is an open access article distributed under the terms and conditions of the Creative Commons Attribution (CC BY) license (<https://creativecommons.org/licenses/by/4.0/>).

1. Introduction

Lagoons cover about 13% of the overall coastal zone worldwide [1]. They are ephemeral systems in a continuous evolution that respond to modifications induced by natural and anthropogenic stressors [2]. Coastal lagoons are among the most valuable environments of the planet, providing a range of ecological, cultural and socioeconomic services [3,4]. Due to the sensitivity of these environments, the lagoons are susceptible to the effects

of climate changes, as documented for many areas worldwide. Extreme events and the global rise of sea levels contributed to coastal inundation and ecosystem losses in the Gulf Coast of Louisiana and Carolina Outer Banks [5], to the loss of habitat of the Jamaica Bay and New York [6] and coastal erosion in Asia and Southeast Asian coasts [7–9]. In the Venice Lagoon, Northern Adriatic Sea, an inestimable cultural heritage is threatened by an increasing frequency of floods from storm surges as a result of regional and man-induced subsidence [10] and rising sea levels [11].

Hydrodynamics and sedimentary processes play a fundamental role in the evolution of lagoons [12–14]. These shallow water bodies are usually formed by a complex network of channels crossing tidal flats and marshlands. Barrier islands partially separate a lagoon from the adjacent coastal waters, while tidal inlets regulate the fluxes of water and sediment with the open sea and, in the long term, the evolution of the internal lagoon areas and the ebb-tidal deltas. Understanding the dynamics of a lagoon, including the exchanges through the tidal inlets, and their effects on the morphology, is of crucial importance for the safeguarding and management of these ecosystems from direct anthropogenic pressures and global changes [15–17].

Although many transitional environments have historic connections with human settlements, the Lagoon of Venice represents a peculiar case as large human modifications of the environment started in the 16th century, contributing to a significant alteration of natural dynamics [16]. Today, the lagoon is becoming increasingly deeper and saltier as it slowly returns to the sea [18], and towards the end of the century, the sea level might rise dramatically, increasing the frequency of inundations, as well as increasing their duration and extent [11]. In response to the present and future threats, the last intervention was the construction of the impressive system of mobile barriers at the three inlets, known as MoSE (from the Italian acronym for “Experimental Electromechanical Module”). The barriers defend the city of Venice and the lagoon islands from water levels of 120 cm over the local datum (approximately 25 cm above the current mean sea level). On 3rd October 2020, the MoSE was operated for the first time during a real flooding scenario, closing the lagoon inlets at 70 cm while the level in the open sea reached a peak of 130 cm [11]. In the next few decades, the increasingly frequent operation of the MoSE will progressively transform the lagoon into a regulated system, which will result in further changes in the hydrodynamics [19], the fluxes of sediments, contaminants and organisms [20] and wetlands morphodynamics [21].

As with most of the transitional areas, the Venice Lagoon is a constantly evolving environment, where the exchanges at the tidal inlets control biological and morphological processes influencing the functionality of the ecosystem and the patterns of erosion and accretion. The fluxes of water and sediment through the Venice Lagoon inlets have been investigated with different approaches over a wide range of temporal and spatial scales [19,22–25]. The average magnitude of tidal exchanges between the Lagoon of Venice and the open sea, determined from time series of flow recorded by acoustic Doppler current profilers (ADCP), equals to $10,000 \text{ m}^3 \text{ s}^{-1}$ [26], and the solid flux estimated by the conversion of acoustic backscatter from ADCP [25] shows a tendency to a loss of sediments for an overall volume of $3.8 \times 10^5 \text{ m}^3 \text{ yr}^{-1}$. The water and sediment exchanges between the sea and the lagoon were also extensively studied using numerical models and validated with in situ data [19,24,27–29], showing that sediment transport through the inlets occurs mostly in suspension, while bedload represents only a limited fraction and is related to bedforms migration [30], likely induced by tidal flow asymmetry [20]. Alterations in sediment transport pathways and erosive processes (e.g., bottom scour) also occur after the recent inlet transformation, as shown by local bathymetric changes of the inlet systems [31].

Since 2004, the morphology of the Venice Lagoon inlets has been strongly modified by the construction of MoSE infrastructures, with consequent changes in both velocity field and sea–lagoon exchanges [32]. Further improvement in the modeling chain is then needed to better understand the effects of these changes within the complex framework of physical processes controlling the sediment budget. Observational strategies still represent

the most straightforward approach to address the study of sediment dynamics in tidal environments. Remote sensing techniques allow the spatial limitations of traditional in situ measurements to be overcome, providing a synoptic view for a better understanding of the relevant surficial processes [33] and for the calibration and validation of sediment transport models [34]. If acoustics represent a useful tool for the studies of transport in the water column, optical remote sensing methods now enable the investigation of sediment transport processes at the surface on a wider spatial scale, providing synoptic maps of suspended sediment distribution [35] on large areas. The frequent revisit time (few days) of current satellite constellations adds a further benefit that is the possibility to investigate the evolution of transport processes in the medium to short-term (i.e., sea storms or river floods) during cloud-free periods.

Few researchers focused on the transport at the inlet in the period from the completion of the MoSE infrastructures (2010) to the start of its operativity (2020); therefore, in addition to theoretical studies, it becomes fundamental to acquire current and updated information on the evolution of the sea–lagoon exchanges with a continuous monitoring of the fluxes of water and sediments through the inlets, and also with investigations on a wider spatial scale to identify sources and pathways of the organic and inorganic particulate transport.

The objective of this work is to test the capability of an integrated method for the autonomous estimate of water and sediment fluxes through the northern inlet of the Lagoon of Venice (Lido inlet). The long-term datasets from the in situ network were analyzed in order to evaluate the temporal variability of suspended sediment in relation to tidal phases and meteo-marine conditions. The capability of this integrated observation system has been tested over a study period of three days, characterized by calm weather conditions when the pattern of resuspension was not affected by wind waves or swells.

2. Study Area

With a total surface of 550 km² and an average depth of about 1 m, the Lagoon of Venice is the largest Mediterranean lagoon and it is morphologically characterized by large extents of shallow areas (tidal and subtidal flats) and marshlands crossed by a complex network of tidal channels (Figure 1). Three inlets (Lido, Malamocco and Chioggia), with variable widths ranging from 350 to 900 m, and depths ranging from 7 to 20 m, ensure water exchanges with the Adriatic Sea, which are driven by a semidiurnal tide with an excursion of about 1 m in spring conditions [20]. Wind can also have a considerable effect on water circulation and exchanges during extreme meteorological events [36]. Two prevailing wind directions are present in the area: northeasterly (Bora), more frequent in winter storms, and southeasterly (Sirocco) more typical of autumn/spring periods [37]. The circulation in the open sea by the Venice Lagoon is characterized by specific patterns generated by the interaction between the coastal current and local tidal dynamics at the inlets [38]. In this context, the Lido inlet (Figure 1, subset A) is a key area within the complex of interactions between the lagoon and the open sea. Two large tidal channels, about 400 m wide, originate from the inlet channel, namely Treporti and San Nicolò (TRP and SN in Figure 1). The two channels are 15 and 7 m deep, respectively, and drain a sector of the lagoon where half of the total water discharge and solid load is vehiculated by the largest tributaries of the drainage basin [39,40]. According to [25], the negative sediment budget of the lagoon is currently dominated by the loss from the Lido inlet, possibly due to the contribution from the input of lagoon tributaries and the erosion of marshlands and tidal flats that still occupy large areas in the northern basin. On the other hand, occasional inputs of marine sediments can be driven by tidal inflow during storm events, when sediments, resuspended and moved by longshore current along the Northern Adriatic coast, are transported and deposited on the flood tidal delta and in the more distal lagoon sectors.



Figure 1. Copernicus Sentinel-2 true-colour composite of the study area at the two tidal channels (San Nicolò—SN, Treporti—TRP) originating from the Lido inlet in the Lagoon of Venice (Northern Adriatic Sea, Italy). In situ data were collected in the 8 sampling stations (pink dots) and the two boat-mounted ADCPs transects (yellow lines). The location of the fixed monitoring stations is also indicated: bottom-mounted ADCPs (red); tidal and meteo gauge Lido Sud station (LS, yellow); and OBS turbidimeters (brown).

Starting from the end of the 19th century, the morphology of the Lido inlet has been subjected to large modifications when jetties were built to stabilize the port channel joining the three preexisting tidal inlets in a single 900 m wide artificial entrance. In the last few decades, the construction of the MoSE system introduced further modifications. On the lagoon side, an artificial island was built at the junction of the TRP and SN channels. The island hosts the buildings of infrastructures to operate the two arrays of barriers, which are hosted in a concrete housing on the seafloor on both channels. On the sea side, at the south of the inlet entrance, a breakwater was successively built, increasing the complexity in the pattern of inflow circulation and outflowing tidal jets [32]. On the northern jetty, a partial restriction of the inlet channel was created to host a navigation lock and two refuge harbors for the transit of boats during the closures of the MoSE mobile barriers. The overall restriction of the inlet channel cross-section increased the current velocities and induced local changes in the inlet sedimentary regime with a transition from depositional to erosive and a net sediment loss in the area of about $612 \times 10^3 \text{ m}^3$ [31].

3. Materials and Methods

This study was based on the integration of data from in situ monitoring networks, field campaigns and satellite-derived products covering the area of the Lido inlet for a period of three days (15–17 September 2020).

Long-term in situ data from field surveys were considered for calibration, intercalibration and validation purposes. Time series from in situ networks were used to investigate the trend of water and sediment fluxes. Tidal level, wind direction and speed were obtained from the time series recorded from the Lido Sud (LS) meteo-marine station (cf. Figure 1) managed by the Municipality of Venice (Centro Previsione e Segnalazione Maree).

3.1. In Situ Monitoring Network

In February 2020, two fixed stations for real-time turbidity monitoring were installed at 2 m depth at the two sides of the artificial island in the Treporti and San Nicolò channels (brown dots in Figure 1). Each station is equipped with an OBS501 turbidity meter (Campbell Scientific, Loughborough, UK) with an integrated antifouling system, which acquires data every 10 min.

Water flow was available from continuous acquisitions of two upward-looking acoustic Doppler current profilers (600 KHz RDI Workhorse Monitor ADCP; Teledyne RD Instruments, San Diego, CA, USA) deployed at the bottom of the inlet channels (red dots in Figure 1), which recorded current velocity and direction and acoustic backscatter along the water column with a 5 min sampling interval and a 0.35 m vertical cell size. Blanking ranges at bottom and surface were excluded from the analysis (2 and 2.5 m, respectively).

3.2. In-Field Activities

Field campaigns were performed at the SN and TRP channels for calibration and intercalibration of the instrumental setup and validation of satellite-derived products. At each station, water turbidity profiles were acquired with an Ocean Seven 316-Plus probe (Idronaut, Brugherio, MB, Italy), equipped with an optical backscatter sensor (Seapoint Sensors, Inc., Exeter, NH, USA). Turbidity data from profiles were used for sensor intercalibration.

An extensive series of transects were acquired with a boat-mounted ADCP in different meteorological and tidal conditions, providing detailed information on the evolution of currents in the TRP and SN sections (yellow lines in Figure 1). The instrument used was a 600 kHz RDI Workhorse Rio Grande ADCP (Teledyne RD Instruments, San Diego, CA, USA) set to operate at a 0.5 m vertical cell size with the exclusion of the surface and bottom blanking ranges, approximately 1 and 2 m, respectively. Instantaneous discharge data from the transects were used for the calibration of the vertically averaged velocities measured by fixed bottom-mounted ADCPs according to the index-velocity method to obtain discharge time series [41]. Moreover, to calculate both time series of water turbidity from the fixed ADCPs and the instantaneous 2-D distribution of water turbidity in the inlet cross-sections recorded during ADCP transects, the acoustic backscatter was converted according to the following procedure. After the acquisition of each transect with the boat-mounted ADCP, profiles of turbidity, temperature and salinity were acquired with the CTD probe on the vertical of the fixed ADCPs, while the boat-mounted ADCP was set to acquisition. The calibration of the acoustic backscatter of both instruments was performed, using the CTD probe data as input for the post-processing with the software Sediview (HR Wallingford, Wallingford, Oxfordshire, UK). The software enables the calculation of water turbidity, starting from the acquired backscatter and water properties (Temperature, Salinity, Turbidity).

Several field surveys were undertaken to gather data for the validation of satellite-derived turbidity. Synchronously to the overpasses of Landsat8 (L8) and Sentinel-2 (S2) satellites, in situ turbidity profiles were carried out with the CTD probe at 8 stations along a transect from the lagoon to the open sea, through the Lido inlet (pink dots in Figure 1). From January 2020, time series of turbidity from fixed monitoring stations were also used for assessing the accuracy of satellite products.

3.3. Remote Sensing Data

In this study, we selected about 50 S2 and L8 images, acquired over the Lagoon of Venice in the period 2017–2020, for validation activities and match-up analysis of water turbidity. S2-A and -B satellite images (Level-1C), processed by ESA (European Space Agency) within the European Union's Copernicus programme, were downloaded from the Copernicus Open Access Hub (<https://scihub.copernicus.eu/> accessed on 12 July 2022), and L8 images were downloaded from the United States Geological Survey (USGS) archive of the Earth Resources Observation and Science (EROS) Center (<http://glovis.usgs.gov> accessed on 12 July 2022). Turbidity maps at 10 m resolution for S2 and 30 m resolution for L8 were

obtained, similarly to [35,42,43]. The acquired imagery was radiometrically calibrated using sensor-specific vicarious gains provided in [44], in order to create a consistent multi-sensor dataset for monitoring aquatic ecosystems, and atmospherically corrected with ACOLITE [Version 20190326.0], applying the dark spectrum approach [45,46]. This approach uses multiple dark targets in the subscene to construct a “dark spectrum” which is used to estimate the atmospheric path reflectance (ρ_{path}) according to the best-fitting aerosol model. Furthermore, the ACOLITE-derived water leaving reflectances ($\rho_w(\lambda)$) were converted into turbidity (T), expressed as a formazin nephelometric unit (FNU), following [47]:

$$T = \frac{A_T^\lambda \rho_w(\lambda)}{(1 - \rho_w(\lambda)/C^\lambda)} \text{ [FNU]}$$

where A_T and C are two wavelength-dependent calibration coefficients. The parameter C was calibrated using “standard” inherent optical properties (IOPs) as described in [48], whereas the A_T coefficient was obtained by a non-linear least-square regression analysis using in situ measurements of T and ρ_w in various European and South American coastal and estuarine environments [47].

From all the available datasets, two S2 and one L8 images were selected to thoroughly analyze turbidity patterns for the three-day period considered by this study (15–17 September 2020). Landsat thermal bands were also processed, according to [49], to derive sea surface temperature (SST) and identify peculiar thermal characteristics of the coastal area.

4. Results and Discussion

Long-term datasets, such as those from bottom-mounted ADCP and turbidity stations, satellite-derived products and data from periodic field measurements, provide a reference base to develop the integrated approach described and discussed here. A previous analysis of precision, uncertainty and representativity of the instrumental setup was carried out. The investigation on the three-day period represents a demonstration case for the study of the dynamics of transport in a complex tidal inlet, with detailed spatial and temporal resolutions.

4.1. Intercalibration of Turbidimeters

For the intercalibration analysis, the turbidity data, averaged from three consecutive measurements (one every ten minutes), from the fixed stations were compared with the mean turbidity measured in the 1–2 m depth-range from CTD probe profiles, acquired in their proximity. A total of 29 and 19 match-ups, respectively, were considered for TRP and SN. The correlations were statistically significant with a coefficient of determination R^2 of 0.98 and 0.96 for the instruments located at TRP and SN, respectively (Figure 2). A good correlation was found throughout the whole sampled range, even if most of the data pairs were localized in the lower part of the calibration range. Suspended sediments in the water column of the Lido inlet are, in fact, typically low and values above 20 FNU are quite uncommon in calm meteo-marine conditions.

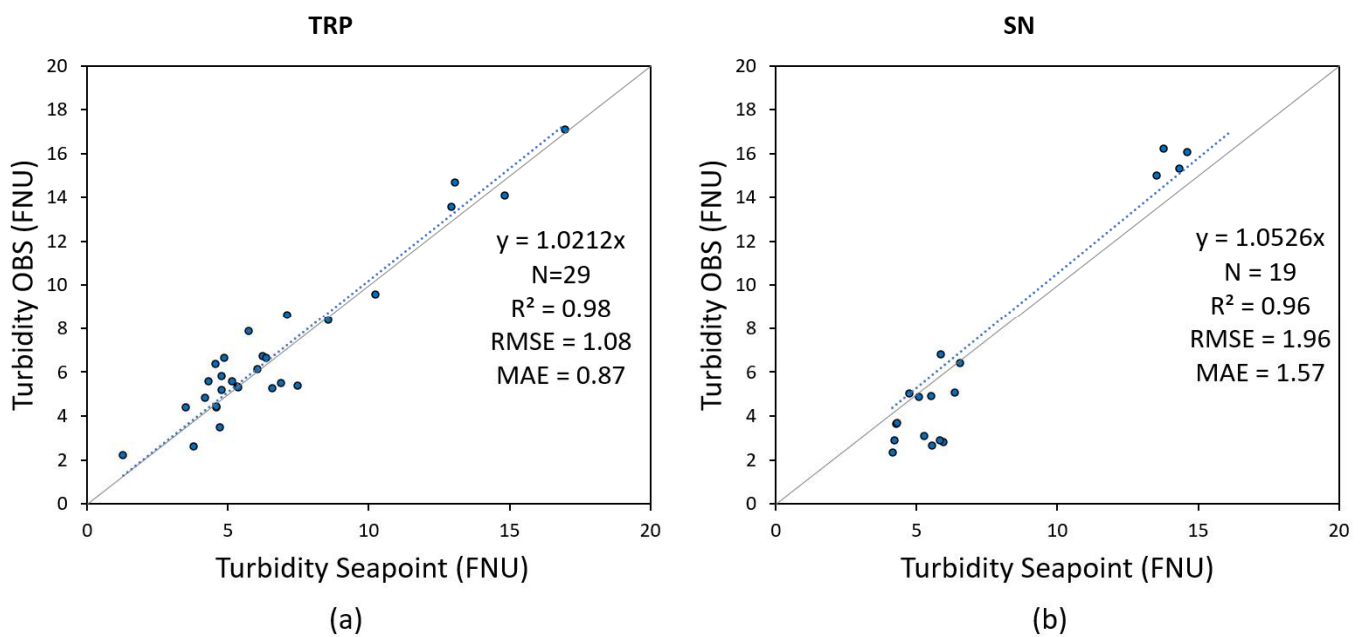


Figure 2. Scatter plot of the turbidity data retrieved from the fixed stations (OBS) compared with the data from CTD probe profiles (Seapoint) at TRP (a) and SN (b). The linear regression equation and the common descriptive statistical metrics are reported in the plots: number of data pairs (N); coefficient of determination (R^2); root mean square error (RMSE); and mean absolute error (MAE). Dotted lines are the best-fit regression, forced through zero. Grey solid line is the 1:1 line.

4.2. Validation of Satellite-Derived Products

The accuracy of turbidity products derived from remote sensing imagery was assessed using in situ data collected at the inlet, synchronously to satellite overpasses. In situ turbidity data include both CTD profiles, acquired during field activities from 2017 to 2021, and continuous data from the fixed stations SN and TRP available from January 2020. The scatter plot in Figure 3 shows the correlation found between satellite-derived turbidity versus in situ measurements for the 199 S2-match-ups and the 96 L8-match-ups with coefficients of determination R^2 of 0.926 and 0.959, for S2 and L8, respectively. This dataset extends the match-up presented in [43], confirming the accuracy assessed for ACOLITE-derived turbidity retrieved from L8 and S2 in the North Adriatic coastal waters [35,50]. In situ turbidity is slightly underestimated by S2 and slightly overestimated by L8; this can be related to the different spatial resolutions of the satellite data, that is 10 m for S2 and 30 m for L8. Overall, these results emphasize the consistency of turbidity derived from L8 and S2 for a quite large quantity of match-ups, as demonstrated in [44]. As seen for data from fixed stations (Figure 2), most of the turbidity values in the lagoon–sea transect ranged in the 2–20 FNU interval.

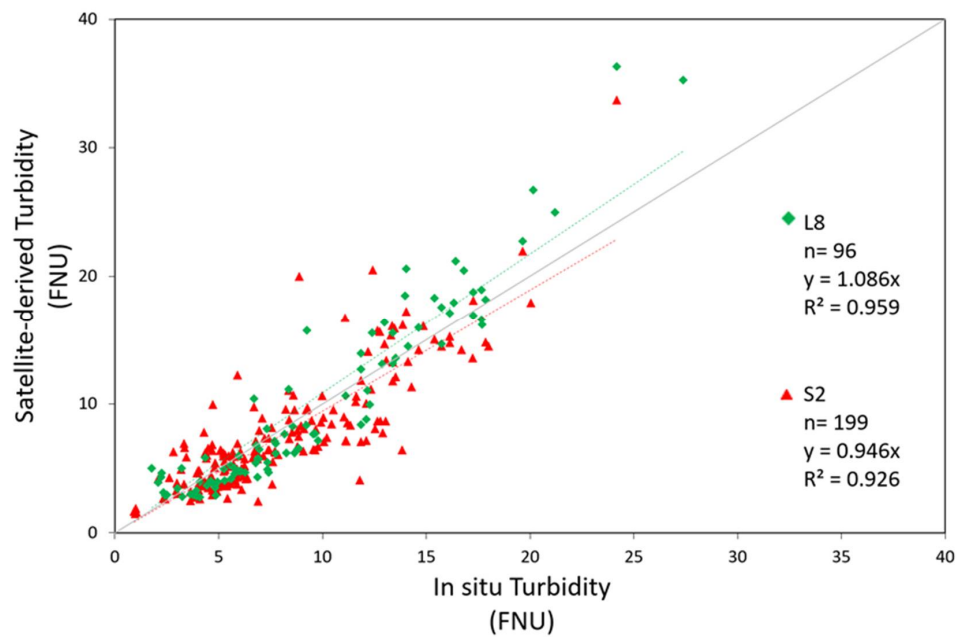


Figure 3. Scatter plot of the L8- and S2-derived turbidity vs. in situ turbidity measurements for 295 match-ups, sampled at the time of the satellite overpasses in 2017–2020. Turbidity values were retrieved according to [47]. Dashed green and red lines are the best-fit regression for L8 and S2, respectively. Grey solid line is the 1:1 line.

4.3. Spatial Turbidity Distribution in the Lagoon–Sea Transect

Figure 4 shows the synoptical distribution of satellite-derived turbidity in the eight stations of the investigated transect (Figure 1, pink dots). Data were subdivided by flood and ebb-tide phases, to emphasize differences in relation to the tidal phase. Excluding the offshore station, which has generally low turbidity (st8), the lagoon–sea transect is characterized by a relatively uniform distribution in the ebb-tide phase, whereas extreme values are more common in the flood. Indeed, flood tide turbidity shows a few outliers for stations located in the inlet channel (st3, st5 and st6) with values up to more than four times the average turbidity. This indicates a larger effect of the flood currents on suspended sediment pattern in the transect, due to the transport of suspended material from the coasts at the north of the inlet by the interaction of longshore drift and flood tidal currents.

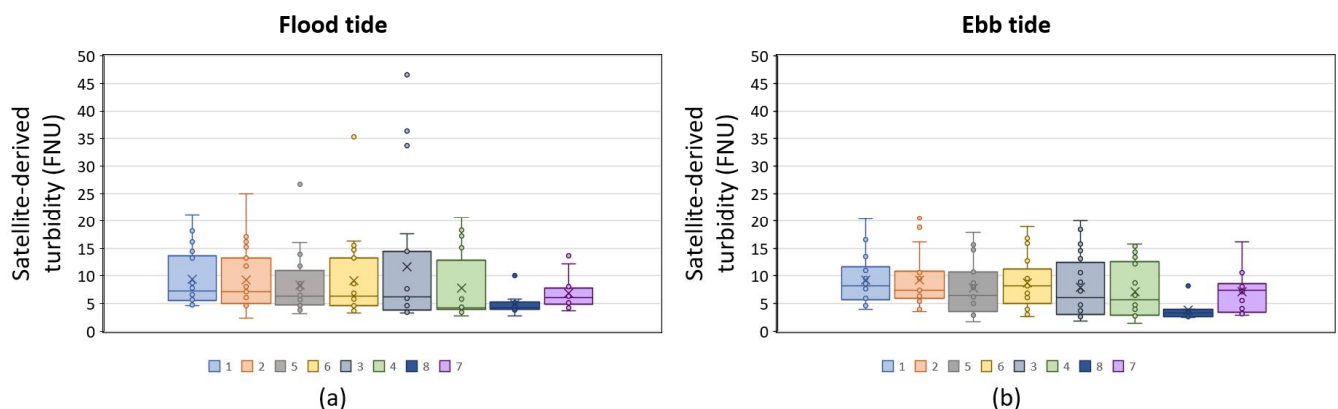


Figure 4. Box-plots of the satellite-derived turbidity in (a) flood and (b) ebb-tide phases for the 8 sampling stations in Figure 1. Stations are ordered following the lagoon–sea transect for SN channel, excluding Station 7, which is located in the TRP channel. The × mark indicates the mean value, the box represents the interquartile range, the line in the box is the median and the whiskers represent the tails of the distribution with external solid points representing the outliers.

4.4. Discharge Calibration

As described in the method section, a regression between instantaneous discharge data from the ADCP transects and the vertically averaged velocities by fixed ADCPs (the index-velocity) is required to calculate the time series of discharge. The correlation between the two variables is quite significant, as shown by the linear regressions presented in Figure 5. The coefficient of determination is close to unity: R^2 is equal to 0.990 for the TRP and 0.988 for SN, therefore, we can assume the index-velocity as a reliable proxy of discharge for both the investigated sections. Furthermore, calibration values cover the typical range of discharges, including those measured during storm surges. As an example, in Figure 6, an excerpt of the discharge time series is reported, showing the second highest water level that occurred during the storm surge of 12th November 2019. Maximum discharges reached $8687 \text{ m}^3 \text{ s}^{-1}$ for the SN and $3672 \text{ m}^3 \text{ s}^{-1}$ for the TRP during flood tide excursion.

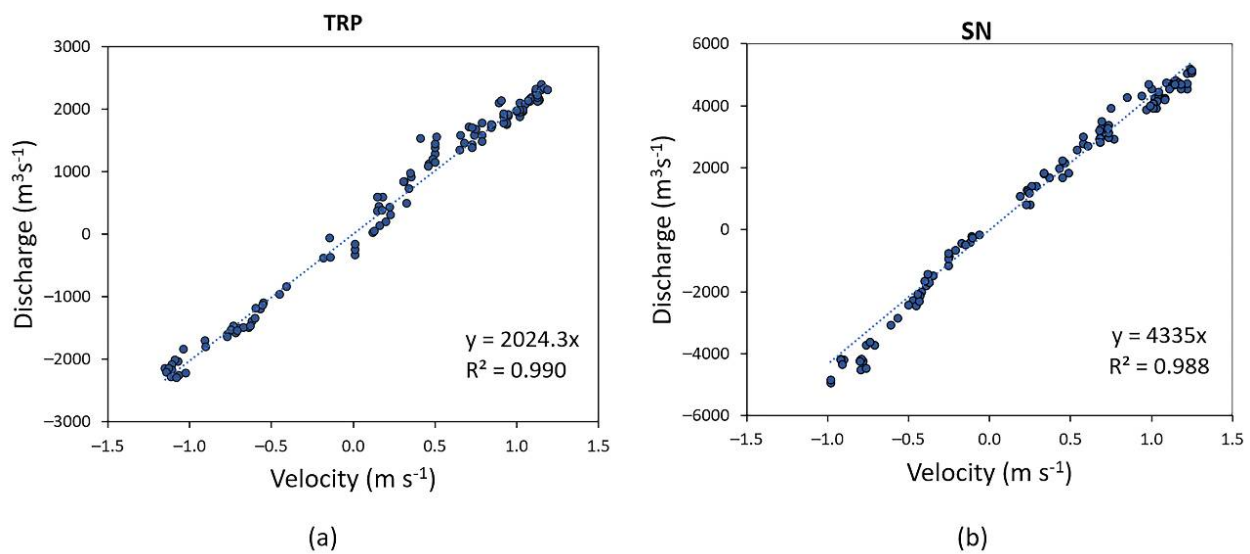


Figure 5. Linear regressions between the vertically averaged velocities by fixed ADCPs (the index-velocity) and instantaneous discharge data from the ADCP transects for the (a) Treporti (TRP) and (b) San Nicolò (SN) stations. Dotted lines are the best-fit regression.

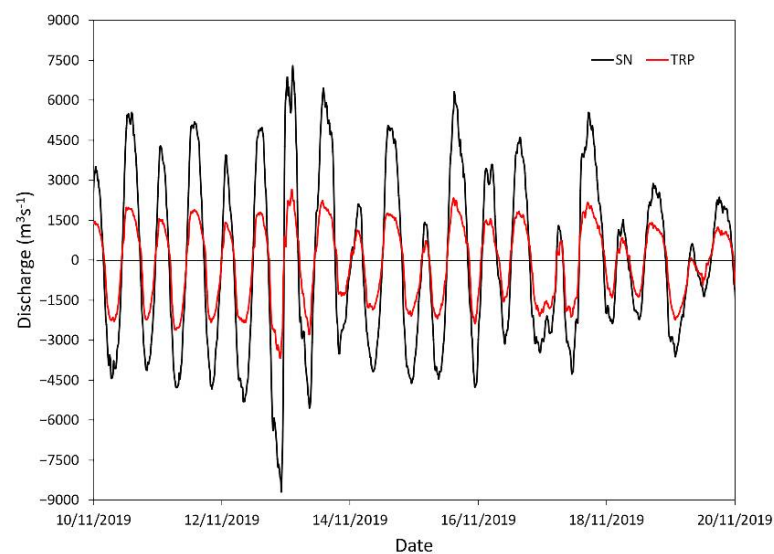


Figure 6. Time series of discharge calculated at TRP and SN channel sections, showing the period of 10–20 November 2019, which includes the second record storm surge of 12 November 2019.

4.5. Long-Term Dataset of In Situ Turbidity, Hydrodynamics and Meteo-Marine Forcing

A 3-month extract (July–September 2020) of the time series of continuous acquisitions from the instrumental network is showed in Figure 7. The plots report water discharge calculated for the two TRP and SN sections, surface turbidity measured at the two fixed monitoring stations and vertically averaged turbidity derived from the conversion of acoustic backscatter from the bottom-mounted ADCPs. Turbidity values extracted from satellite maps at the two fixed stations were superimposed on the surface turbidity plot. The figure also shows tide level and wind speed and direction recorded at Lido Sud station. This 3-month interval was selected because it includes representative tidal conditions and interesting meteo-marine events, and cloud-free satellite images were available. Unfortunately, in this period the ADCP at TRP had to be removed for maintenance (8 July till 7 August), interrupting the data continuity, whereas for the ADCP at SN backscatter data was not available from 14th to 30th July.

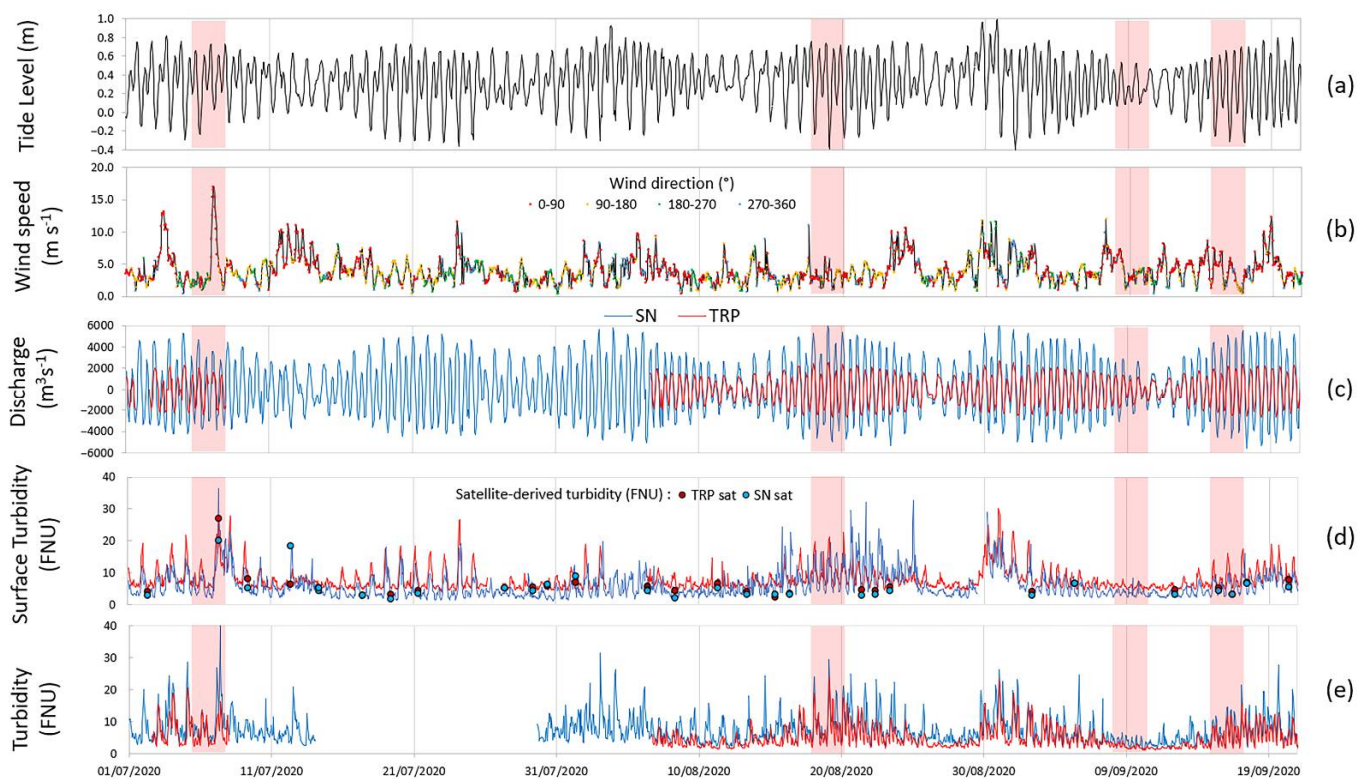


Figure 7. July–September 2020: hourly time series of tidal level (a) and wind speed and direction (red = 0° – 90° , yellow = 90° – 180° , green = 180° – 270° , cyan = 270° – 360°) (b), measured at the Lido Sud station; time series of discharge estimated with the index-velocity method from data of the bottom-mounted ADCPs (positive values of discharge indicate a seaward flow) (c); time series of surficial turbidity measured at fixed TRP and SN stations (circles represent turbidity values extracted from satellite maps at the two stations) (d); the vertically averaged turbidity derived from the conversion of acoustic backscatter from the bottom-mounted ADCPs (e). Red areas mark the periods described and discussed in text.

During the time interval in Figure 7, the trends of surficial and vertically averaged turbidity in the two sections are very similar and are mainly modulated by the semidiurnal tide excursion and by the spring–neap tidal cycle. The amplitude of the observed variations is, generally, higher during spring tides and lower during neap tides. As visible in the Figure 8 left panel, referred to the period 18–20 August 2020, the most pronounced turbidity peaks generally correspond to the ebb-tide phase. The lowest variations are instead found during neap tides, such as, for instance, the period 8–10 September 2020, Figure 8 right panel. This evidence combined with the trend of discharge suggests a tendency to a loss of

suspended sediments from the lagoon in normal conditions, which is also confirmed by the vertically averaged turbidity derived from the ADCPs backscatter.

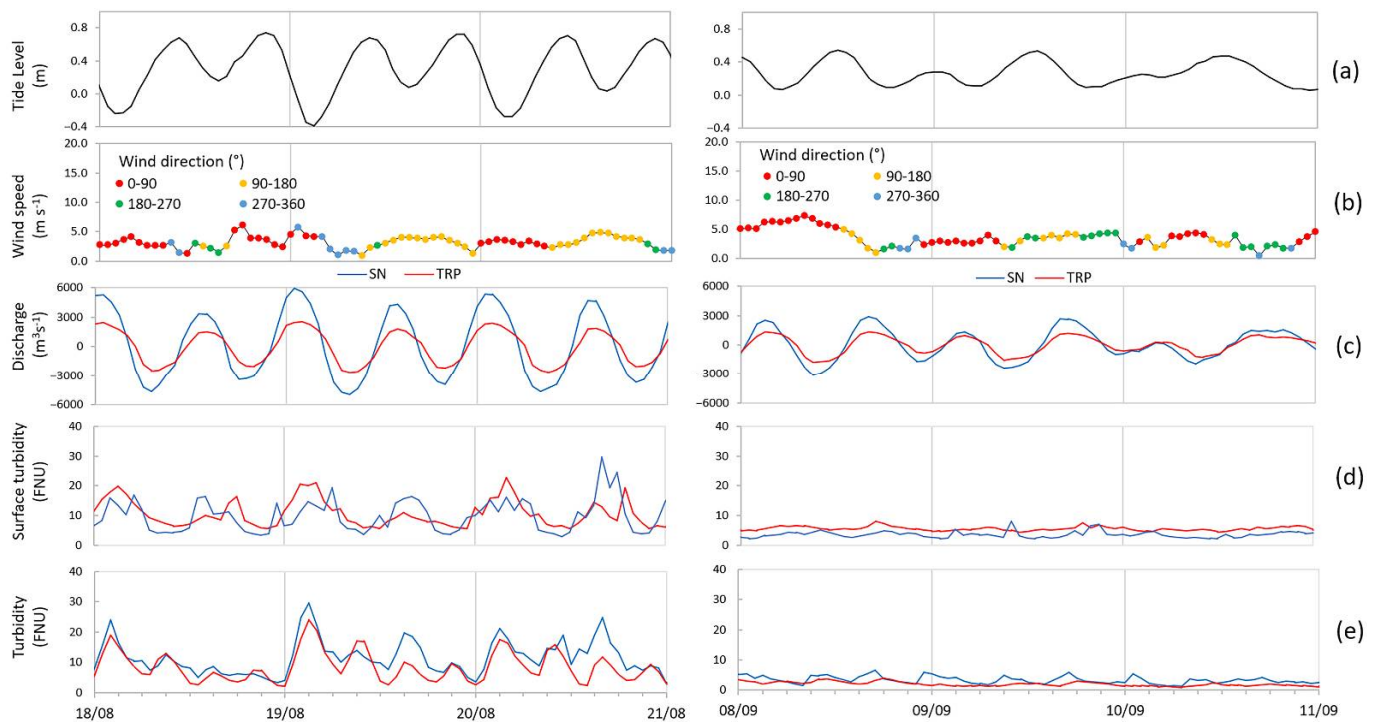


Figure 8. Subset of the time series presented in Figure 7. Left panel: from 18th to 20th August 2020. Right panel: from 8th to 10th September. Hourly time series of tidal level (a) and wind speed and direction (red = 0°–90°, yellow = 90°–180°, green = 180°–270°, cyan = 270°–360°) (b), measured at the Lido Sud station; time series of discharge estimated with the index-velocity method from data of the bottom-mounted ADCPs (positive values of discharge indicate a seaward flow) (c); time series of surficial turbidity measured at fixed TRP and SN stations. (d); the vertically averaged turbidity derived from the conversion of acoustic backscatter from the bottom-mounted ADCPs (e).

The effect of meteo-marine forcing was also noticeable in the time series in Figure 7, even if the time window did not include particularly strong meteorological events. Only during the 5–7 July 2020 event, the wind speed was higher than 15 m s⁻¹ for a few hours (Figure 9). During this event, bora wind at Lido Sud station reached 17.7 m s⁻¹ on 7 July at 3:00 AM. The flow associated to flood tide-induced surface turbidity peaks at SN and TRP fixed turbidimeters (36.4 and 25.9 FNU, respectively) around 8:00 AM, whereas vertically averaged turbidity from ADCPs backscatter slightly differed in the two stations. At SN, two consecutive peaks were recorded: the first reached 27 FNU at 3:00 AM during the maximum wind intensity and at the late ebb-tide phase, the second reached a value of 40 FNU at 9:00 AM and corresponded to the early flood tide phase during the period of maximum current velocity. While the second peak represented the transport related to flood tide currents, the effect of which is measured also at the surface, the first peak was mainly related to the bottom shear stress associated with tidal currents and it was not detected by surficial fixed turbidimeter. At TRP, the vertically averaged turbidity slightly increased up to 18 FNU, but did not exhibit a clear signal of wind effects as visible at the surface.

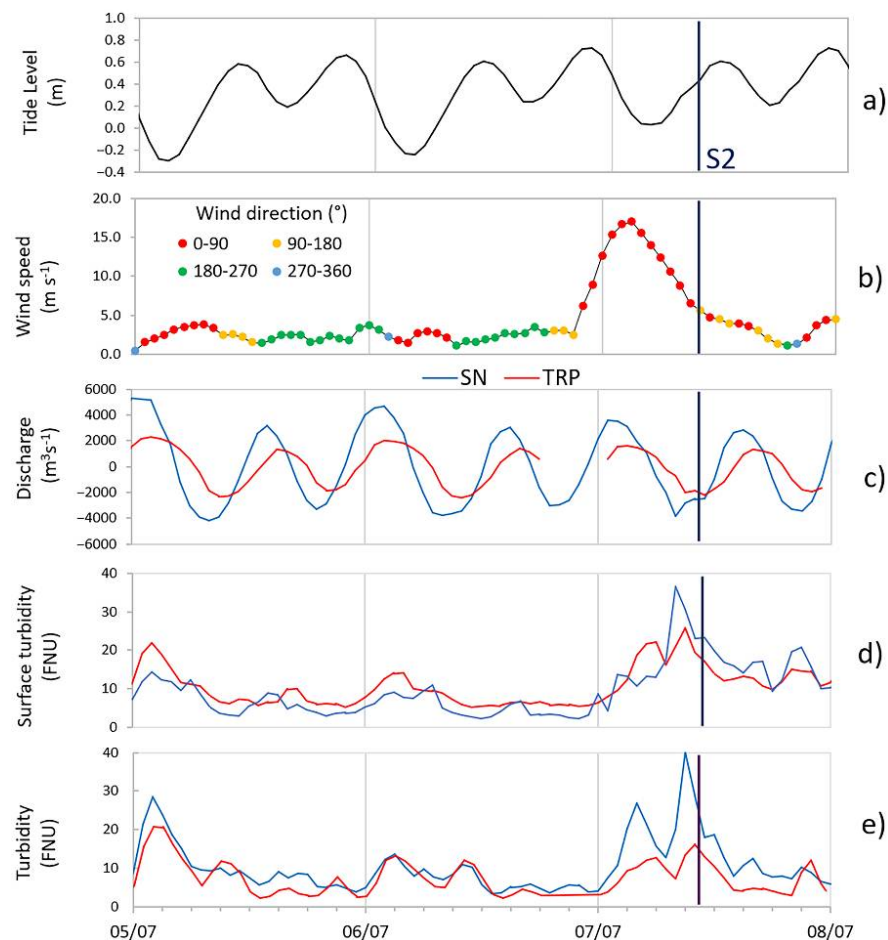


Figure 9. Subset of the time series presented in Figure 7 for the period from 5 to 7 July 2020. Hourly time series of tidal level (a) and wind speed and direction (red = 0° – 90° , yellow = 90° – 180° , green = 180° – 270° , cyan = 270° – 360°) (b), measured at the Lido Sud station; time series of discharge estimated with the index-velocity method from data of the bottom-mounted ADCPs (positive values of discharge indicate a seaward flow) (c); time series of surficial turbidity measured at fixed TRP and SN stations (d); and the vertically averaged turbidity derived from the conversion of acoustic backscatter from the bottom-mounted ADCPs (e). Vertical blue line marks the S2 satellite overpass time.

Periods of intense wind, particularly bora, such as in the case of 5–7 July 2020 (Figure 9), determine the occurrence of relatively higher turbidity peaks associated to the flood tidal phases that transport into the lagoon not only sand at the bottom, but also a significant amount of fine suspended particles at the surface, as visible in the records of fixed turbidimeters. According to [25], bora winds with intensities higher than 9 m s^{-1} significantly affect the suspended particle transport at the Lido inlet and the adjacent littoral at north, as well as the shallow-water areas within the northern lagoon basin. The north littoral represents an important source of suspended sediments for the Lido inlet: materials resuspended and mobilized on the beaches and in the shoreface are transported longshore and enter the inlet following the flood currents and transporting the suspended load for a long distance into the flood-tidal delta and inner lagoon areas [21]. The northern lagoon basin has larger terrestrial inputs from the Dese River and the Silone Channel—the two main freshwater tributaries of the drainage basin [39]. Moreover, it is characterized by large mud-flats and saltmarshes, which are more susceptible to resuspension by wind waves than the other parts of the lagoon. These morphological characteristics of the northern lagoon basin strongly influence the sediment transport through the Lido inlet, since the area is mainly drained by the TRP channel.

Overall, the analysis of the time series emphasizes that surficial turbidity and vertically averaged turbidity from the bottom-mounted ADCPs are controlled by hydrodynamics and meteo-marine conditions, as demonstrated in [19,25–28].

4.6. Demonstration Case of 15–17 September 2020. Test of the Integration of the Analyzed Variables

For the period of three days (15–17 September 2020), an integrated analysis of data from the in situ monitoring networks, field campaigns and satellite-derived products, was performed to study the evolution of suspended sediment fluxes. This period was characterized by relatively calm weather with moderate meteo-marine conditions (maximum wind speed less than 8 m s^{-1} from NE-E for the whole period). As discussed in Section 4.5, once natural external forcing such as wind and waves are excluded, the transport dynamics in the inlets is only driven by the tidal currents and the trend of fluxes are mainly modulated by the tidal signal, in particular by the semidiurnal tide. In the investigated period, tidal circulation was characterized by a spring tide with a marked diurnal inequality and with a maximum excursion of about 1.1 m in the night phase (Figure 10a). Wind speed was always lower than 7 m s^{-1} with variable directions ranging from north-west to south (Figure 10b). For the station TRP, the trend of discharge, estimated from the index-velocity regression (Figure 5), showed a slight asymmetry towards the ebb phase. The maximum instantaneous discharges were about $5500 \text{ m}^3 \text{ s}^{-1}$ at SN and $2300 \text{ m}^3 \text{ s}^{-1}$ at TRP, for an overall discharge of $7800 \text{ m}^3 \text{ s}^{-1}$ through the Lido inlet channel (Figure 10c). The trends of turbidity measured at fixed TRP and SN stations were quite similar and clearly modulated by the tide. Relatively higher values were found at TRP, where the average was 8.3 FNU, compared to 5.5 FNU at SN (Figure 10d). Turbidity peaked during the ebb-tide phase with the highest observed values in correspondence to the maximum tidal excursions, typically about 2 h after the occurrence of discharge and velocity peaks. At TRP, maximum turbidity values reached 17.5 FNU at 3:00 AM on 17 September. A peak of 16.5 FNU was also observed at SN on the same day in correspondence to the maximum discharge in the flood tidal phase. The vertically averaged turbidity from ADCPs backscatter (Figure 10e) reached values of 15.3 FNU at TRP and 21 FNU at SN during the peak of water discharge on 17 September.

The satellite-derived turbidity maps of the period 15–17 September (Figure 11) provide a synoptic view of the turbidity pattern in the whole investigated area at the time of each daily overpass, around 10:00 AM. The turbidity values retrieved from the satellite images in proximity of the fixed stations ranged between 3 to 6 FNU and were consistent with the range measured by the turbidimeters at the time of the satellite overpasses (blue vertical lines in Figure 10d). There was a slight difference in turbidity between SN and TRP channels with a delta of about 2 FNU that is observable from both the satellite turbidity maps and the time series of turbidity measured at fixed stations, indicating that the difference represents an environmental variation and not an instrumental bias. Although the satellite acquisitions were around the late flood/early ebb-tide phase in the three days, the three scenes represented slightly different hydrodynamical conditions, because of the about 45 min daily delay of the astronomical tide, local lag and flow inertia. On 15 September, the image was acquired 1:30 h after the high tide at the Lido Sud tide gauge station: the measured flow was still entering at TRP ($-271 \text{ m}^3 \text{ s}^{-1}$) while it was already ebbing at SN ($651 \text{ m}^3 \text{ s}^{-1}$) (Figure 10c). This opposite behaviour is typical of the two channels at the flow reversal and is due to a different inertia of the two sub-basins. On the 16th and on the 17th, the flow entered both channels and the discharge magnitude increased with the increasing tide delay (-972 at TRP and $-976 \text{ m}^3 \text{ s}^{-1}$ at SN on 16th; -1477 at TRP and $-1668 \text{ m}^3 \text{ s}^{-1}$ at SN on 17th).

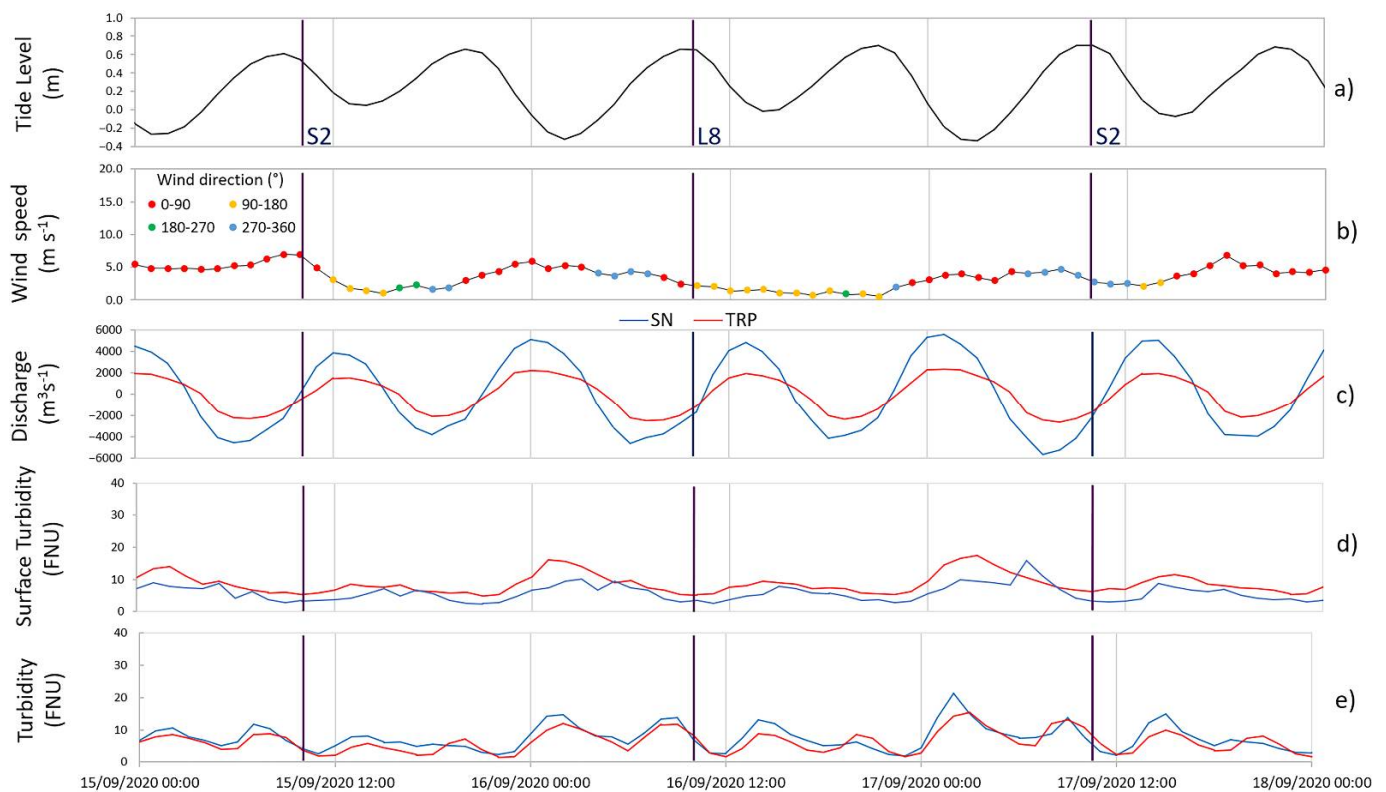


Figure 10. Subset of the time series presented in Figure 7 for the period from 15 to 17 September 2020: tide level measured at Lido Sud meteo-marine station (a); wind speed and direction (red = 0° – 90° , yellow = 90° – 180° , green = 180° – 270° , cyan = 270° – 360°) (b); time series of discharge estimated with the index-velocity method from data of the bottom-mounted ADCPs; positive values of velocity and discharge indicate a seaward flow (c); time series of surficial turbidity measured at fixed TRP and SN stations (d); and the vertically averaged turbidity derived from the conversion of acoustic backscatter from the bottom-mounted ADCPs (e). Vertical blue lines mark the satellites overpass time. S2: Sentinel-2; L8: Landsat 8.

The maps of Figure 11 show how the hydrodynamics influenced turbidity distribution in the investigated area: a positive gradient is observable along the tidal channels moving from the sea to the internal sectors of the lagoon. Higher values of turbidity, up to 15 FNU, were estimated around the city of Venice and the island of Murano, possibly related to sediment resuspension by water traffic around and alongside the main channels as already observed by [43]. In the inlet channel, turbidity values on the 15th and 16th were quite similar to those of the open sea (3–6 FNU) where relatively calm conditions prevailed. This is particularly evident also in the true-colour images where natural bottom features such as nearshore parallel bars and artificial structures such as submerged breakwaters on the coast and the MoSE mobile barriers at the bottom of TRP are visible (see Supplementary Materials Figure S1). The more intense flow on the 17th determined the formation of turbulent wakes in the inlet channel, in correspondence to the head of the southern jetty and in the lee of MoSE structures, marked by trails of higher turbidity. The central part of the inlet channel was instead characterized by less turbid water from the open sea flowing through the deeper pass between the tip of the northern jetty and the breakwater. South of the inlet, a complex turbid pattern was also observable, which was originated by interaction of the outflowing jet with the longshore current and the artificial structure of the breakwater in the previous tidal cycle.

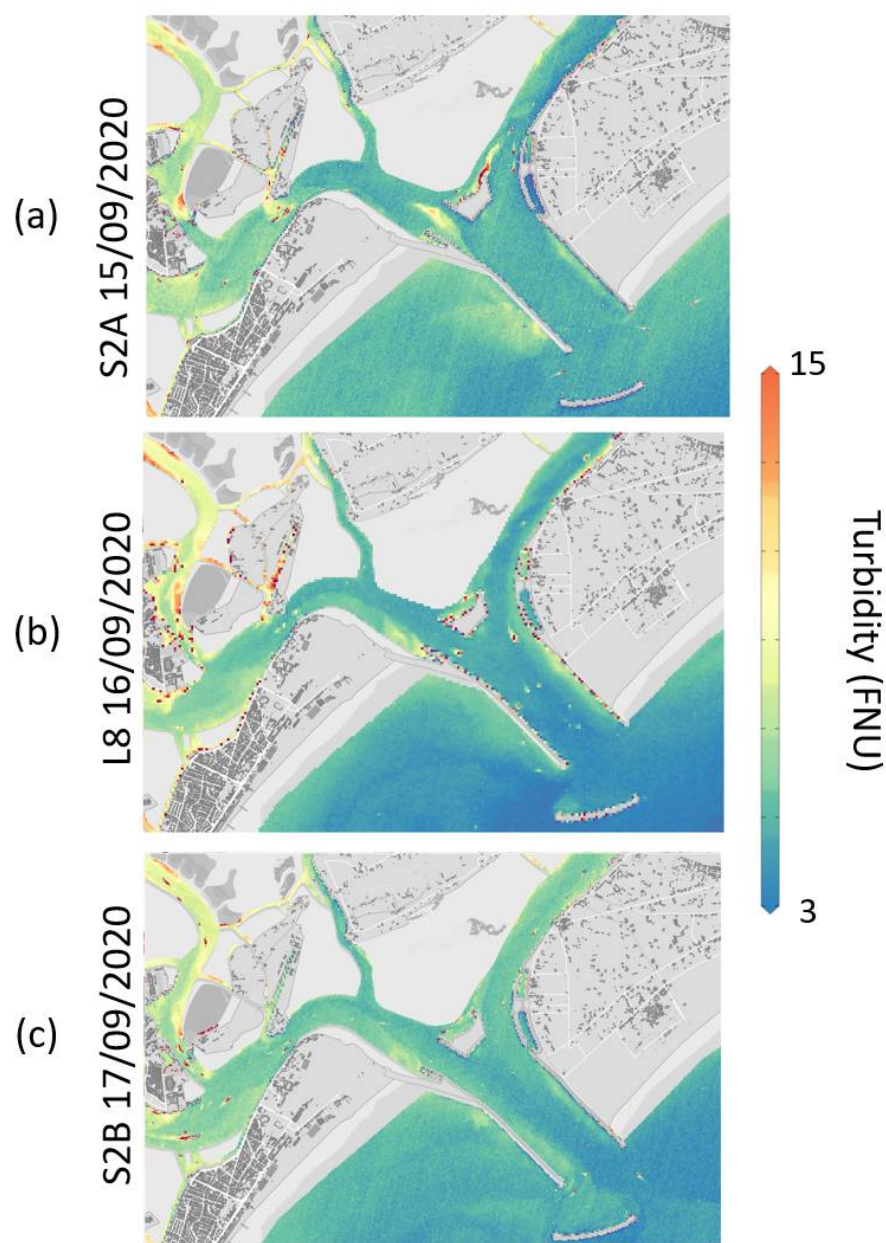


Figure 11. Satellite-derived turbidity maps of the study area for the investigated period: panel (a) Sentinel-2A 15 September 2020; panel (b) Landsat 8 16 September 2020; and panel (c) Sentinel-2B 17 September 2020.

The spatial resolution of the maps also permits the identification of small-scale details such as the plumes of sediment resuspension (turbidity up to 14 FNU) generated by dredging activities and visible in the proximity of the MoSE structures, close to the artificial island, on 15 September. Interestingly, the dispersion of two plumes followed the same opposite direction of the flow in the two channels.

Satellite images provide information on the surface water layer with a synoptic view of the whole study area. However, the integration of in situ data from all sources with the satellite-derived turbidity maps adds in-depth information on the water column, allowing the description of the three-dimensional pattern of suspended sediment transport. Figure 12 shows the interpolation of CTD profiles acquired on 15 September along the lagoon–sea transect (white dotted line in Figure 1). The sections of salinity, temperature and turbidity show a well-mixed water column, a condition that extended up to St3, located 5 km along the transect in the lagoon–sea direction. In the proximity of the St4 located just outside

the inlet, a buoyant plume of colder and relatively fresher water (24.3 °C and 32 psu, averaged values between 1 to 3 m of depth) was observable. This feature was related to the transport of water from rivers, located northeast of Lido inlet, which was driven by the coastal current, as visible in the satellite-derived SST maps of 15th and 16th September in Supplementary Materials Figure S2. Beneath this structure, a salt wedge characterized by typical seawater salinity and a relatively warmer temperature was visible (24.8 °C and 35.5 psu) and extended seaward all the way to St8. The buoyant plume did not affect turbidity, which remained quite low along the transect, from the lagoon to the open sea, with values within 7.5 FNU and no significant trend was measured along the water column. These results were consistent with the corresponding satellite derived product.

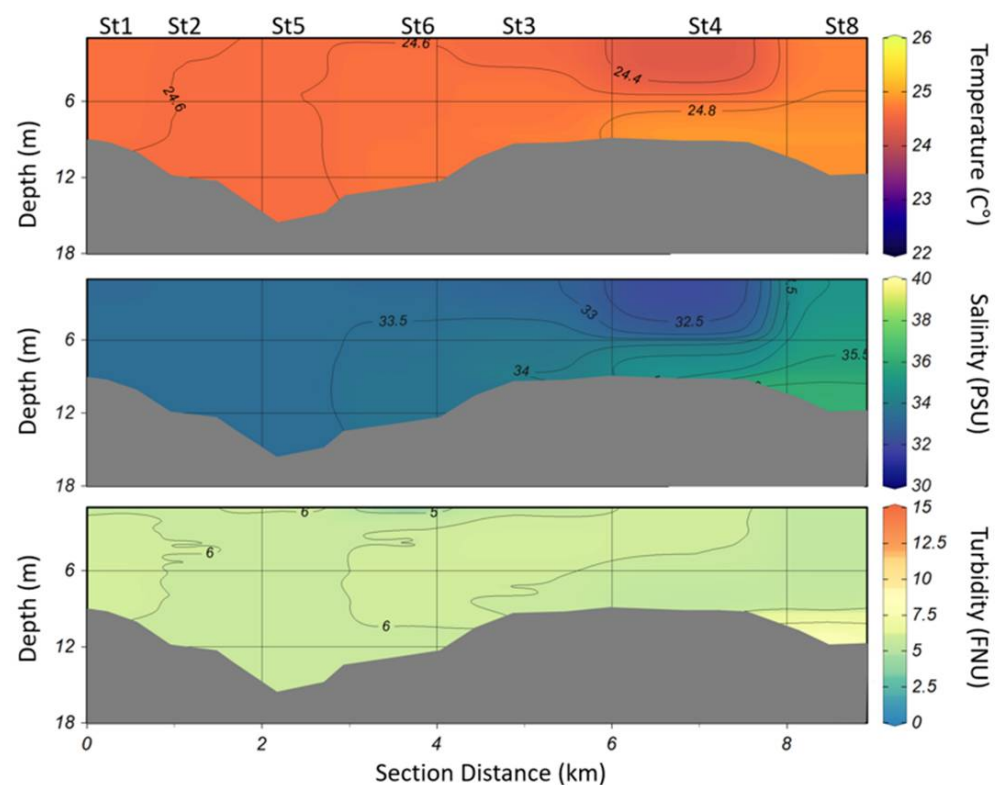


Figure 12. Representations of CTD casts (temperature, salinity and turbidity) along the lagoon–sea transect (white dotted line in Figure 1) on 15 September 2020. Plot generated with Ocean Data View software (<https://odv.awi.de>, 2021 accessed on 12 July 2022).

During the ADCP acquisitions along the TRP and SN transects on 16th and 17th September, profiles of temperature, salinity and turbidity were measured over the bottom-mounted ADCPs, at the centre of the channels (see Figure 1). The results are represented as a time series in the Figure 13. The profiles were acquired hourly from 8:00 AM to 1:00 PM in the late flood/ebb-tide phase. On 16 September, the evolution of the water parameters in the two sections was similar: salinity along the water column was rather constant and a slight difference was visible (Δ Salinity = 0.6 psu) both for the TRP and SN channels (Figure 13a,b). Minor differences in temperature (Δ Temperature \leq 0.5 °C) were observed with a relative progressive increase in the whole profile with the arrival of water from the inner lagoon heated by solar radiation over the shallow areas. A similar behaviour was displayed by the temperature also on 17 September, while a saltier structure (34.75 psu) was present in the bottom layer from 9:00 to 12:00 AM (Figure 13c,d). In both the measured intervals, turbidity increased during the ebb phase in the whole water column. A more complex evolution was observed at TRP where the resuspension by the shear stress at the maximum flow determined higher turbidity in the bottom layer.

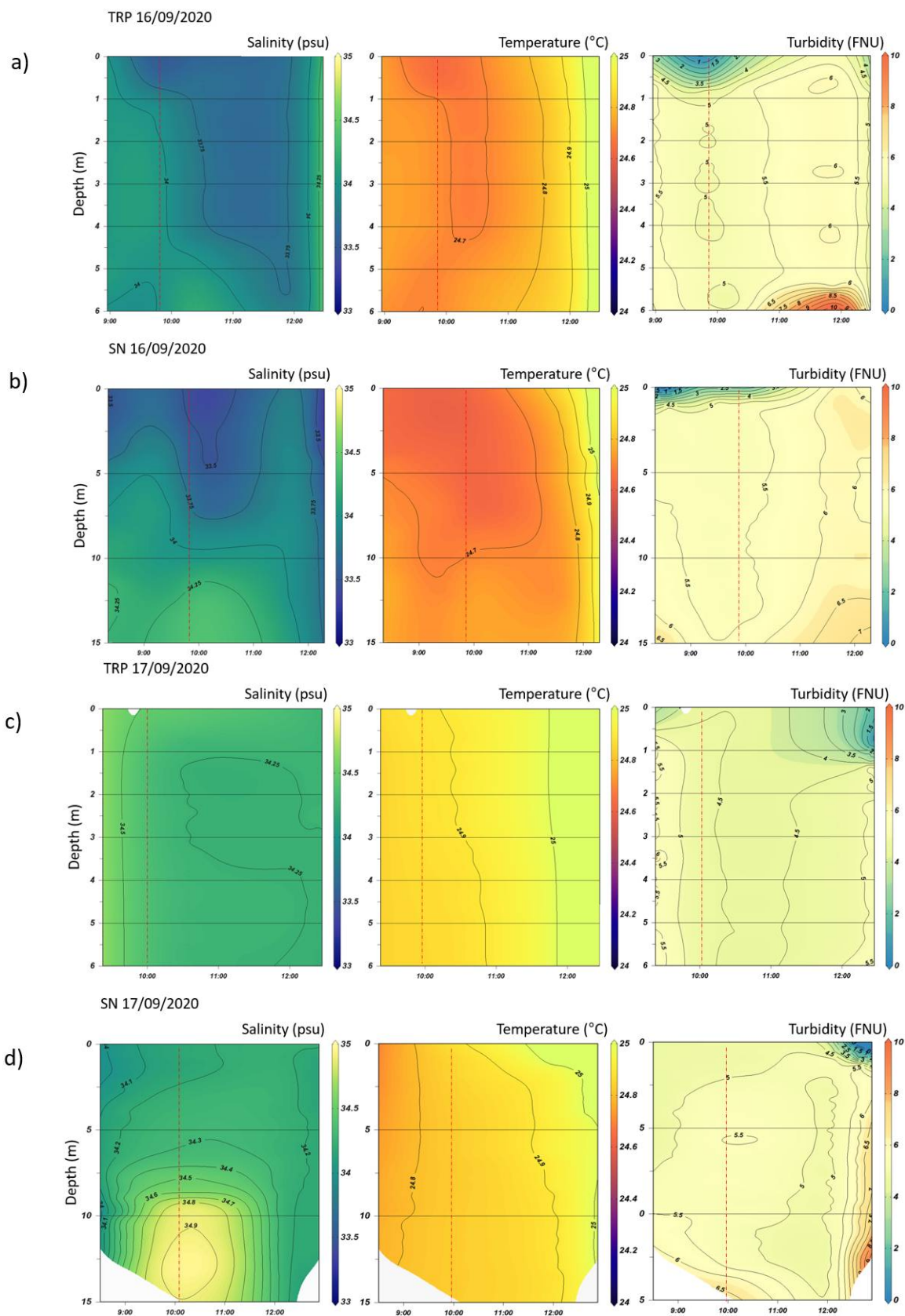


Figure 13. Time series of salinity, temperature and turbidity from CTD casts acquired over the fixed ADCPs at the TRP and SN sections on 16th ((a,b) respectively) and 17th ((c,d) respectively) September 2020. Vertical red dashed lines mark the satellites overpass time. Plot generated with Ocean Data View software (<https://odv.awi.de>, 2021 accessed on 12 July 2022).

Turbidity data obtained from the conversion of backscatter of the boat-mounted ADCP along SN and TRP transects permitted the investigation of the pattern of suspended transport in the two sections. Figure 14 shows the turbidity transects acquired synchronously to the satellite overpass on 16 and 17 September. In both the visualized situations, the water column is well-mixed with minor spatial differences in the distribution of suspended particles. Relatively higher turbidity was evident on the NE side of the TRP channel (Δ turbidity of 1.5 FNU). This is a typical feature of the Lido inlet, which is strictly related to the resuspension of bottom sediments due to the shallow depth of this side of the channel. Coherent patterns were also visible at the surface on satellite-derived products (Figure 11) and reported on in the results of previous research [25].

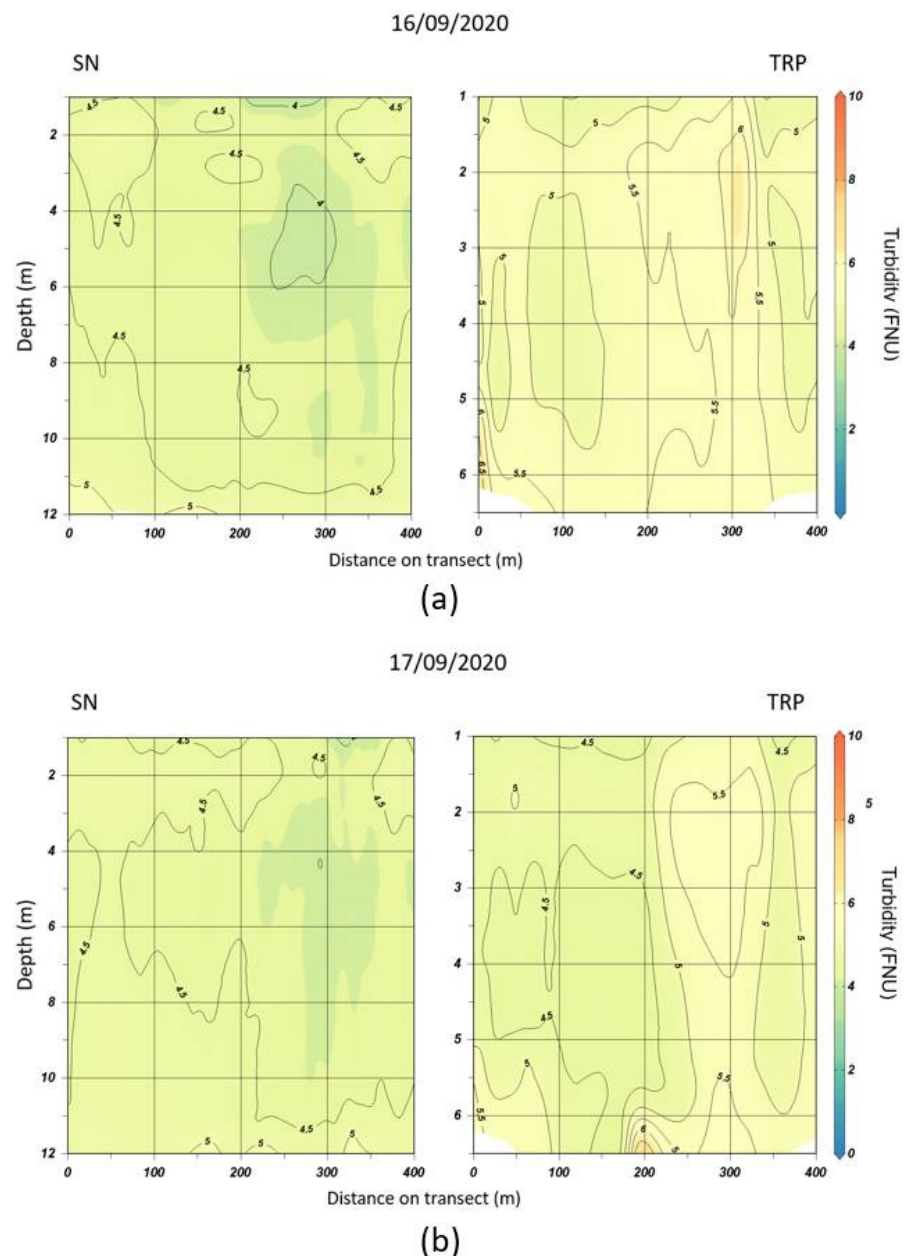


Figure 14. Turbidity values along the transects in sections SN (left panels) and TRP (right panels) (panel a) measurements done on 16 September 2020 (9:40 AM SN transect, 10:00 AM TRP transect) and in (panel b) 17 September 2020 (10:02 AM SN transect, 10:23 AM TRP transect) September 2020. The direction of all the transects is SW to NE. Plot generated with Ocean Data View software (<https://odv.awi.de>, 2021 accessed on 12 July 2022).

The time series of turbidity along the water column of the TRP and SN channels obtained from the backscatter conversion of the two bottom-mounted ADCPs are shown in Figure 15. Values ranged from 2 to 25 FNU with a gradient along the water column. Higher turbidity was typically recorded in the bottom layers especially in the ebb-tidal phase when the water flow was stronger, even in the absence of meteo-marine forcings. Turbidity reached maximum values at TRP, where the resuspension can extend to the upper water layers. It is also quite evident that the higher values were associated with the main tide excursions following the trend of diurnal inequality of the tidal signal on the flow. For both stations, the surficial layer was characterized by the same interval of variation recorded by the turbidimeters of the fixed stations.

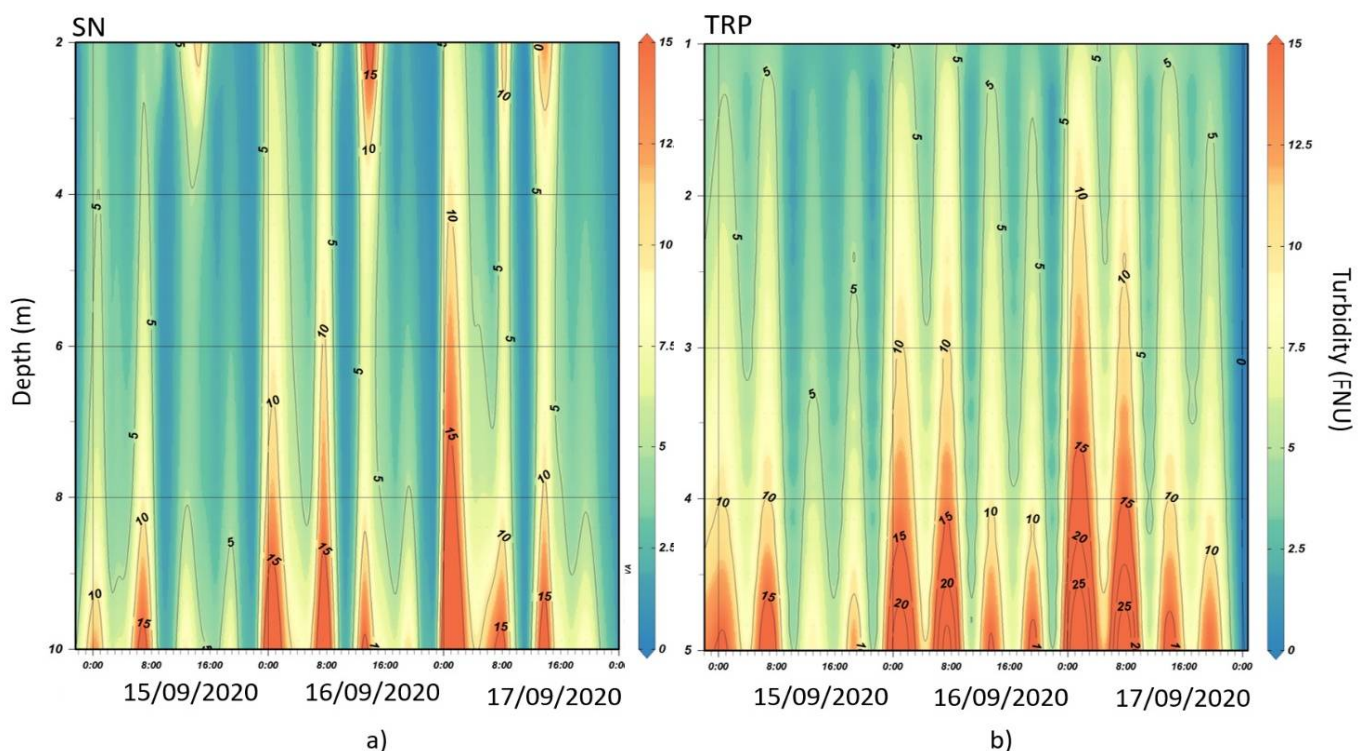


Figure 15. Time series of turbidity derived from acoustic backscatter of the two bottom-mounted ADCPs along the water column for the three-day test-period: (a) SN and (b) TRP. The y-axis scale is set according to the different depths of the two channels. Plot generated with Ocean Data View software (<https://odv.awi.de>, 2021 accessed on 12 July 2022).

The time series in Figure 15 shows that the turbidity in the ebb-tide phase was higher at TRP than SN, similarly to the trend of fixed turbidimeters reported in Figure 10, panel d. This may be a result of the peculiar morphology of the northern basin of the lagoon, drained by the Treporti Channel [51], where the larger extension of saltmarshes, and tidal and subtidal flats are more susceptible to erosion and can potentially supply more suspended particles [25]. Moreover, the northern lagoon basin also has larger terrigenous inputs that are vehiculated in the lagoon by the two main tributaries of the drainage basin [39]. The few observed pulses in the concentration of turbidity at the surface of SN station (Figure 15a) were likely related to the plume of sediment from ongoing dredging activities in the area, as visible on satellite images (Figure 11).

The uncertainties of the adopted methodology were evaluated on the basis of long-term datasets for both remote sensing and in situ acoustic techniques. The accuracy of satellite-derived products was assessed by comparing the in situ and estimated data in the validation procedure, as discussed above (Figure 3). To assess the quality of data derived from acoustic backscatter, the errors of the calibration procedure for each bottom-mounted ADCP were considered (Figure 16). The scatter plots of measured turbidity versus

turbidity estimated from the conversion of backscatter from bottom-mounted ADCPs (left panels) show a good correlation (R^2 equal to 0.841 for TRP and 0.845 for SN). The plots of the measured turbidity versus error ratio, calculated as the ratio between estimated and measured turbidity (right panels), show that the calibration is acceptable, with error ratio generally close to 1, except for the lowest concentration range, where uncertainty is larger due to the variable organic/inorganic particulate content. Indeed, the choice of a three-day relatively calm period restricts the values of turbidity to the lowest range where data dispersion is higher. However, it has the advantage of showing the potential and the limits of the methodology in the most common conditions when tidal currents are the dominant factor driving suspended sediment transport. At higher concentrations, typical of storm conditions, the correlations between estimated and measured values generally improve because of the predominant presence of the inorganic particulate that results in a stronger signal-to-noise ratio [25].

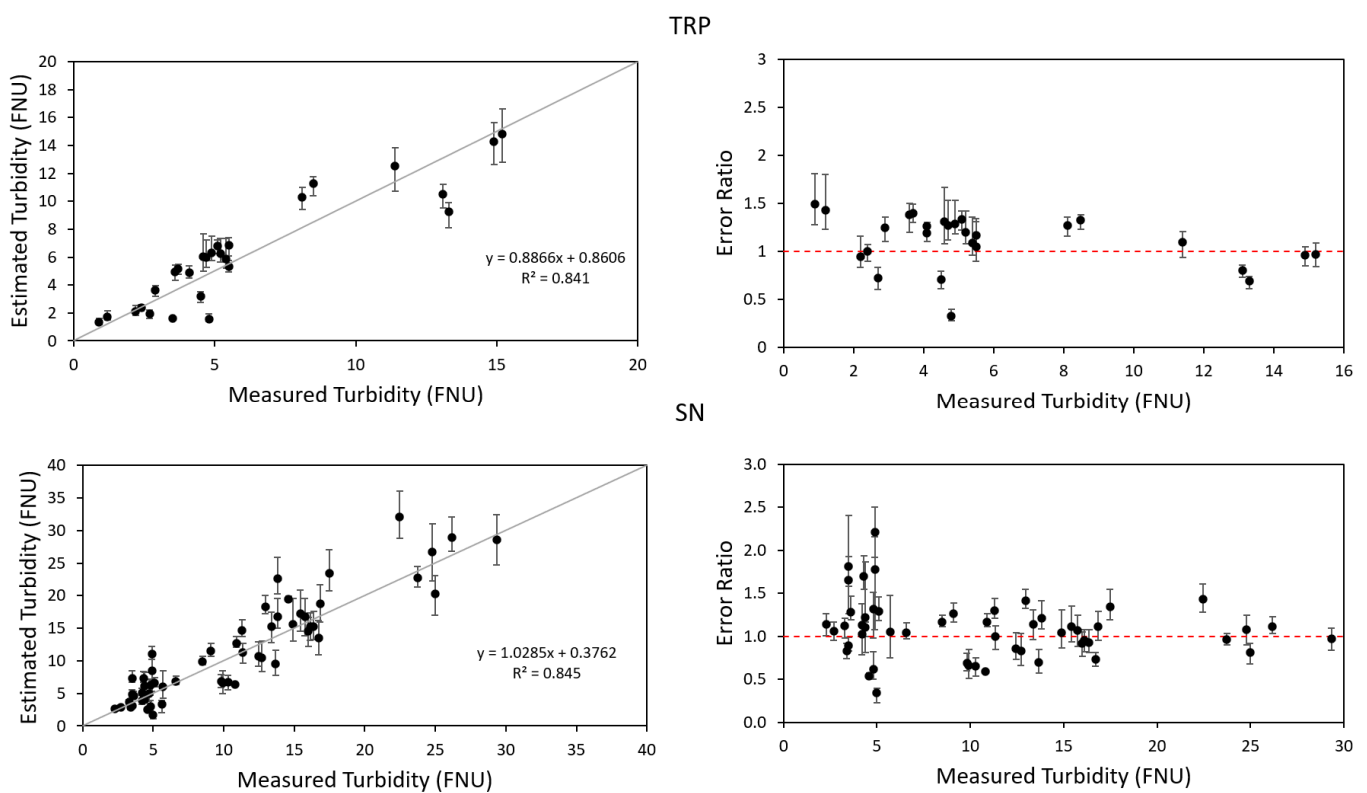


Figure 16. (Left) panels: scatter plot of measured turbidity versus turbidity estimated from the conversion of backscatter from bottom-mounted ADCPs for TRP and SN stations. (Right) panels: plots of the measured turbidity versus error ratio for TRP and SN stations. Grey solid lines are the 1:1 lines; the red dashed line represents the error ratio equal to 1. The black dots represent 4-beam averaged turbidity from ADCP data. The error bars in all plots represent the range of the four ADCP beams estimates (min and max values).

4.7. Application of the Implemented Methodology to the 5–7 July 2020 Meteo-Marine Event

In Figure 9, we showed the surface and vertically averaged turbidity continuously measured by the instrumental network during the 5–7 July 2020 event. Figure 17 provides the satellite-derived map of the synoptic distribution of turbidity in the inlet area and the time series of turbidity along the water column of the TRP and SN channels, obtained from the conversion of backscatter of the two bottom-mounted ADCPs.

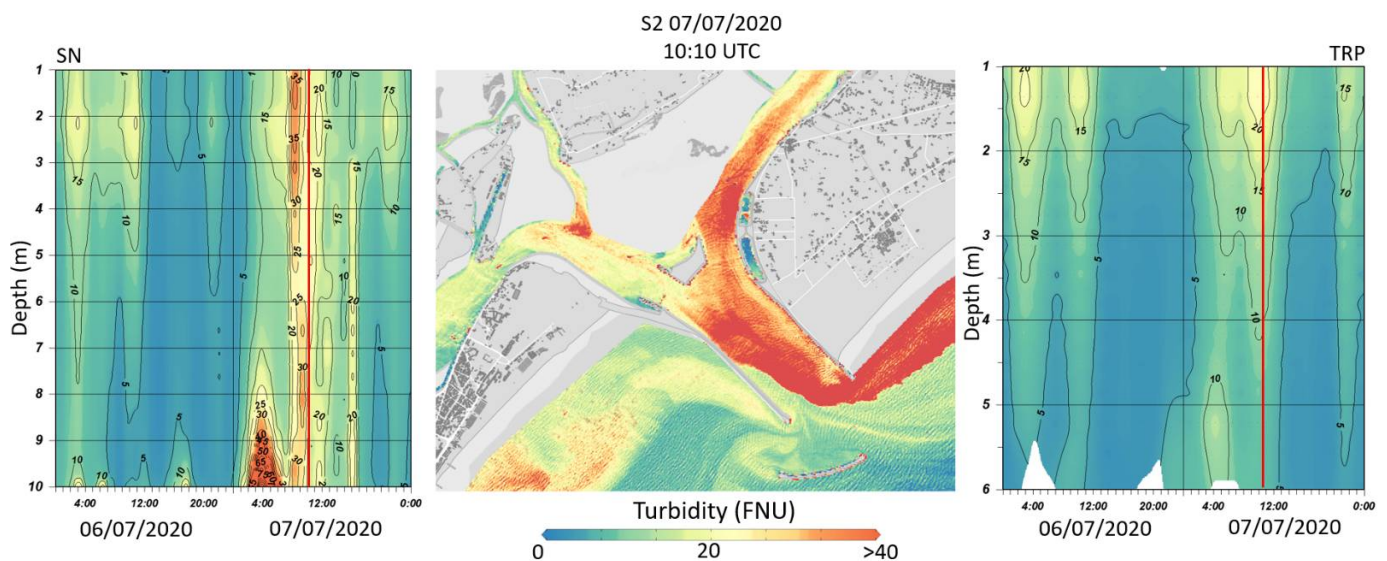


Figure 17. Wind event 6–7 July 2020. (Central) panel: satellite-derived turbidity map of the study area for the investigated period. (Left, right) panels: time series of turbidity derived from acoustic backscatter of the two bottom-mounted ADCPs along the water column for SN (left) and TRP (right) stations. Vertical red lines mark the S2 satellite overpass time.

The scene represented in the turbidity map shows the surficial patterns of suspended sediment and enables the inferring of information on the transport processes at different spatial scales in these typical wind conditions. The intense sediment resuspension on the coast caused by the action of waves on the shoreface is particularly evident. One interesting feature is the clear-cut boundary of the area, where materials resuspended from the coast were transported by longshore current, which seems to imply a limited exchange between this coastal belt (approximately 1 km) and the open sea. Close to the inlet mouth, the flood tidal current drags this turbid belt into the main channel from which the particulate is distributed into the lagoon channel network. This confirms and supports the interpretation of the continuous dataset and emphasizes the important role of storm-driven sediment supply on the morphodynamics of wetlands, as also discussed by [21].

During the satellite overpass and image acquisition, the TRP channel received the larger fraction of suspended sediments at the surface, while the SN channel had lower turbidity values. This can be related to a peculiar hydrodynamic condition originated by a test of the MoSE barriers, which determined the partial closure of the SN channel in the time interval around image acquisition. The sheltered area at south-west of the inlet was characterized by a markedly lower range of turbidity. Yet, in this area, the patterns of turbidity highlighted the trend of currents around the jetty and the artificial breakwater.

The panels on both sides of the map represent the time series of turbidity along the water column of the TRP and SN channels during the meteo-marine event. The intense pulse of suspended material caused by the wind event overlapped to the regular modulation of turbidity values along the column by the tidal currents. For the SN section, the surface values were consistent to those of the turbidity map and fixed turbidimeter at the time of overpass, whereas TRP values were underestimates. This is likely due to the position of the bottom-mounted ADCP, which was slightly marginal in respect to the flow line.

5. Conclusions

In this work we demonstrated the capability of an integrated methodology for the investigation of water and sediment transport in a tidal inlet with detailed spatial and temporal resolutions. By combining satellite-derived turbidity, continuous data from a network of monitoring instruments, instantaneous measurements of current velocity and

acoustic backscatter, we obtained a 3-D reconstruction of suspended sediment patterns in the northern inlet of the Venice Lagoon. Satellite-derived turbidity proved to be useful for describing the surficial evolution of the lagoon–sea exchanges through the inlets, defining the suspended sediment distribution and dispersion pathways and tracing their origin and fate. Turbidity features at relatively fine spatial scale, such as small turbulent structures, as well as the effects of anthropic stresses such as dredging activities, were also clearly detected. With the recent launch of Landsat 9, combined with Landsat 8 and Sentinel-2 A/B, the aquatic science and end-user community can benefit from high-quality and consistent satellite-derived products for operational purposes at a one-to-three-day revisit time.

As a paradigm of an extremely valuable environment at risk, the Lagoon of Venice represents a particularly interesting case study for sediment dynamics in response to natural forcing and man-made morphological transformations. In this context, there is an urgent need to find accurate, reliable and cost-efficient monitoring techniques to assess the impact of the recent construction of flood defence structures, such as the MoSE mobile barriers. The integrated system described and discussed here will be soon implemented in the other two inlets of Malamocco and Chioggia. Once completed, the observing network will enable the assessment of short-to-long-term variations on sediment transport pathways, the exploitation and enhancement of the existing data infrastructures and, real-time ancillary data permitting, also the assessment of the effects of moderate-to-extreme meteo-marine events. By adding in-depth observations, a robust and dense dataset will be available, providing more detailed and consistent information for the characterization of morpho-hydrodynamic processes. The multitude of available observational data might be of great help for research on aquatic science and for the end-user community. For instance, numerical models, which are usually based on simplified assumptions and do not necessarily reflect the actual complexity of natural processes, can be considerably improved by higher spatial and temporal resolution data. The ecosystem management practices will also benefit from these data for operational purposes, such as the monitoring of inlet morphological transformations and erosion and the planning of coastal defence. After the extensive morphological interventions operated at the Venice Lagoon inlets, and with the expected scenarios of sea level rise, the developed approach can also help to understand how the future regulation of the inlet flow introduced by the operation of the flood barriers will affect the sediment fluxes and, in the long term, the lagoon morphodynamics.

Supplementary Materials: The following supporting information can be downloaded at: <https://www.mdpi.com/article/10.3390/rs14143371/s1>, Figure S1: satellite true-color images of the study area for the investigated period: (panel a) Sentinel-2 15 September; (panel b) Landsat 8 16 September; and (panel c) Sentinel-2 17 September. Figure S2: sea surface temperature (SST) maps derived from Landsat 7 and Landsat 8 sensors, acquired on 15 and 16 September, respectively. Both scenes show a belt of relatively colder water ($\Delta T = 0.8$ °C) originating from the jets of river mouths located on the northern sector of the Adriatic Sea and moving southward following the local coastal current.

Author Contributions: G.M.S.: conceptualization, methodology, writing—review and editing, formal analysis, investigation. F.B.: conceptualization, methodology, writing—review and editing, formal analysis, investigation. G.M.: review and editing, formal analysis, investigation. G.L.: formal analysis, investigation. L.Z.: conceptualization, methodology, writing—review and editing, formal analysis, investigation. All authors have read and agreed to the published version of the manuscript.

Funding: Scientific activities were performed with the contribution of the Provveditorato for the Public Works of Veneto, Trentino Alto Adige and Friuli Venezia Giulia, provided through the concessionary of State Consorzio Venezia Nuova and coordinated by CORILA in the framework of the Venezia2021 Research Program. This work was also carried out in the context of the CERTO (Grant agreement No. 870349) project, funded by the European Union’s Horizon 2020 research and innovation program.

Data Availability Statement: All data are fully available without restriction.

Acknowledgments: The authors wish to thank L. Dametto for technical support during sampling and other fieldwork, and the crew of the M/B “Litus”, G. Zennaro, D. Penzo, M. Penzo and R.

Vianello. Hydro-meteorological data covering the study area were provided by the Centro Previsione e Segnalazione Maree, Municipality of Venice. The European Space Agency and the European Union's Copernicus program are thanked for the acquisition and free distribution of Sentinel-2 images used in this work and we thank the U.S. Geological Survey and Earth Resources Observation and Science (EROS) Center for Landsat 7 and Landsat 8 data. We are grateful to RBINS for making ACOLITE publicly and freely available. We are grateful to the three anonymous reviewers for helpful suggestions and comments on the manuscript.

Conflicts of Interest: The authors declare that they have no known competing financial interests or personal relationships that could have appeared to influence the work reported in this paper. The funders had no role in the design of the study; in the collection, analyses, or interpretation of data; in the writing of the manuscript; or in the decision to publish the results.

References

1. Cohen, J.E.; Small, C.; Mellinger, A.; Gallup, J.; Sachs, J. Estimates of Coastal Populations. *Science* **1997**, *278*, 1209–1213. [[CrossRef](#)]
2. Fletcher, C.A.; Spencer, T. *Flooding and Environmental Challenges for Venice and Its Lagoon: State of Knowledge*; Cambridge University Press: Cambridge, UK, 2005; ISBN 978-0-521-84046-0.
3. Gonenc, I.E.; Wolflin, J.P. *Coastal Lagoons: Ecosystem Processes and Modeling for Sustainable Use and Development*; CRC Press: New York, NY, USA, 2004; ISBN 978-0-429-20926-0.
4. Newton, A.; Brito, A.C.; Icely, J.D.; Derolez, V.; Clara, I.; Angus, S.; Schernewski, G.; Inácio, M.; Lillebø, A.I.; Sousa, A.I.; et al. Assessing, Quantifying and Valuing the Ecosystem Services of Coastal Lagoons. *J. Nat. Conserv.* **2018**, *44*, 50–65. [[CrossRef](#)]
5. Anthony, A.; Atwood, J.; August, P.; Byron, C.; Cobb, S.; Foster, C.; Fry, C.; Gold, A.; Hagos, K.; Heffner, L.; et al. Coastal Lagoons and Climate Change: Ecological and Social Ramifications in U.S. Atlantic and Gulf Coast Ecosystems. *Ecol. Soc.* **2009**, *14*, 29. [[CrossRef](#)]
6. Brown, K.M.; Tims, J.L.; Erwin, R.M.; Richmond, M.E. Changes in the nesting populations of colonial waterbirds in Jamaica Bay wildlife refuge, New York, 1974–1998. *Northeast. Nat.* **2001**, *8*, 275–292. [[CrossRef](#)]
7. Cai, F.; Su, X.; Liu, J.; Li, B.; Lei, G. Coastal Erosion in China under the Condition of Global Climate Change and Measures for Its Prevention. *Prog. Nat. Sci.* **2009**, *19*, 415–426. [[CrossRef](#)]
8. Besset, M.; Anthony, E.J.; Brunier, G.; Dussouillez, P. Shoreline Change of the Mekong River Delta along the Southern Part of the South China Sea Coast Using Satellite Image Analysis (1973–2014). *Géomorphologie Relief Process. Environ.* **2016**, *22*, 137–146. [[CrossRef](#)]
9. Zhang, Y.; Hou, X. Characteristics of Coastline Changes on Southeast Asia Islands from 2000 to 2015. *Remote Sens.* **2020**, *12*, 519. [[CrossRef](#)]
10. Zanchettin, D.; Bruni, S.; Raicich, F.; Lionello, P.; Adloff, F.; Androsov, A.; Antonioli, F.; Artale, V.; Carminati, E.; Ferrarin, C.; et al. Sea-Level Rise in Venice: Historic and Future Trends (Review Article). *Nat. Hazards Earth Syst. Sci.* **2021**, *21*, 2643–2678. [[CrossRef](#)]
11. Lionello, P.; Nicholls, R.J.; Umgiesser, G.; Zanchettin, D. Venice Flooding and Sea Level: Past Evolution, Present Issues, and Future Projections (Introduction to the Special Issue). *Nat. Hazards Earth Syst. Sci.* **2021**, *21*, 2633–2641. [[CrossRef](#)]
12. Thorne, P.D.; Hardcastle, P.J.; Flatt, D.; Humphery, J.D. On the Use of Acoustics for Measuring Shallow Water Suspended Sediment Processes. *IEEE J. Ocean. Eng.* **1994**, *19*, 48–57. [[CrossRef](#)]
13. Holdaway, G.P.; Thorne, P.D.; Flatt, D.; Jones, S.E.; Prandle, D. Comparison between ADCP and Transmissometer Measurements of Suspended Sediment Concentration. *Cont. Shelf Res.* **1999**, *19*, 421–441. [[CrossRef](#)]
14. Gartner, J.W. Estimating Suspended Solids Concentrations from Backscatter Intensity Measured by Acoustic Doppler Current Profiler in San Francisco Bay, California. *Mar. Geol.* **2004**, *211*, 169–187. [[CrossRef](#)]
15. Kirwan, M.L.; Megonigal, J.P. Tidal Wetland Stability in the Face of Human Impacts and Sea-Level Rise. *Nature* **2013**, *504*, 53–60. [[CrossRef](#)] [[PubMed](#)]
16. Solidoro, C.; Bandelj, V.; Bernardi, F.; Camatti, E.; Ciavatta, S.; Cossarini, G.; Facca, C.; Franzoi, P.; Libralato, S.; Canu, D.; et al. Response of the Venice Lagoon Ecosystem to Natural and Anthropogenic Pressures over the Last 50 Years. In *Coastal Lagoons*; Kennish, M., Paerl, H., Eds.; Marine Science; CRC Press: Boca Raton, FL, USA, 2010; Volume 20103358, pp. 483–511. ISBN 978-1-4200-8830-4.
17. Newton, A.; Icely, J.; Cristina, S.; Brito, A.; Cardoso, A.C.; Colijn, F.; Riva, S.D.; Gertz, F.; Hansen, J.W.; Holmer, M.; et al. An Overview of Ecological Status, Vulnerability and Future Perspectives of European Large Shallow, Semi-Enclosed Coastal Systems, Lagoons and Transitional Waters. *Estuar. Coast. Shelf Sci.* **2014**, *140*, 95–122. [[CrossRef](#)]
18. Ackroyd, P. *Venice: Pure City*; Talese, N.A., Ed.; Doubleday: New York, NY, USA, 2009.
19. Ferrarin, C.; Cucco, A.; Umgiesser, G.; Bellafiore, D.; Amos, C.L. Modelling Fluxes of Water and Sediment between Venice Lagoon and the Sea. *Cont. Shelf Res.* **2010**, *30*, 904–914. [[CrossRef](#)]
20. Ferrarin, C.; Tomasin, A.; Bajo, M.; Petrizzo, A.; Umgiesser, G. Tidal Changes in a Heavily Modified Coastal Wetland. *Cont. Shelf Res.* **2015**, *101*, 22–33. [[CrossRef](#)]
21. Tognin, D.; D'Alpaos, A.; Marani, M.; Carniello, L. Marsh resilience to sea-level rise reduced by storm-surge barriers in the Venice Lagoon. *Nat. Geosci.* **2021**, *14*, 906–911. [[CrossRef](#)]

22. Gačić, M.; Mancero Mosquera, I.; Kovačević, V.; Mazzoldi, A.; Cardin, V.; Arena, F.; Gelsi, G. Temporal Variations of Water Flow between the Venetian Lagoon and the Open Sea. *J. Mar. Syst.* **2004**, *51*, 33–47. [[CrossRef](#)]
23. Bianchi, F.; Ravagnan, E.; Acri, F.; Bernardi-Aubry, F.; Boldrin, A.; Camatti, E.; Cassin, D.; Turchetto, M. Variability and Fluxes of Hydrology, Nutrients and Particulate Matter between the Venice Lagoon and the Adriatic Sea. Preliminary Results (Years 2001–2002). *J. Mar. Syst.* **2004**, *51*, 49–64. [[CrossRef](#)]
24. Bellafiore, D.; Umgiesser, G.; Cucco, A. Modeling the Water Exchanges between the Venice Lagoon and the Adriatic Sea. *Ocean Dyn.* **2008**, *58*, 397–413. [[CrossRef](#)]
25. Defendi, V.; Kovačević, V.; Arena, F.; Zaggia, L. Estimating Sediment Transport from Acoustic Measurements in the Venice Lagoon Inlets. *Cont. Shelf Res.* **2010**, *30*, 883–893. [[CrossRef](#)]
26. Gačić, M.; Kovačević, V.; Mazzoldi, A.; Paduan, J.; Arena, F.; Mosquera, I.M.; Gelsi, G.; Arcari, G. Measuring Water Exchange between the Venetian Lagoon and the Open Sea. *Eos Trans. Am. Geophys. Union* **2002**, *83*, 217–222. [[CrossRef](#)]
27. Tambroni, N.; Seminara, G. Are Inlets Responsible for the Morphological Degradation of Venice Lagoon? *J. Geophys. Res. Earth Surf.* **2006**, *111*. [[CrossRef](#)]
28. Umgiesser, G.; De Pascalis, F.; Ferrarin, C.; Amos, C.L. A Model of Sand Transport in Treporti Channel: Northern Venice Lagoon. *Ocean Dyn.* **2006**, *56*, 339. [[CrossRef](#)]
29. Carniello, L.; D’Alpaos, A.; Defina, A. Modeling wind waves and tidal flows in shallow micro-tidal basins. *Estuar. Coast. Shelf Sci.* **2011**, *92*, 263–276. [[CrossRef](#)]
30. Madricardo, F.; Fogliani, F.; Kruss, A.; Ferrarin, C.; Pizzeghello, N.M.; Murri, C.; Rossi, M.; Bajo, M.; Bellafiore, D.; Campiani, E.; et al. High Resolution Multibeam and Hydrodynamic Datasets of Tidal Channels and Inlets of the Venice Lagoon. *Sci. Data* **2017**, *4*, 170121. [[CrossRef](#)]
31. Toso, C.; Madricardo, F.; Molinaroli, E.; Fogarin, S.; Kruss, A.; Petrizzo, A.; Pizzeghello, N.M.; Sinapi, L.; Trincardi, F. Tidal Inlet Seafloor Changes Induced by Recently Built Hard Structures. *PLoS ONE* **2019**, *14*, e0223240. [[CrossRef](#)]
32. Ghezzi, M.; Guerzoni, S.; Cucco, A.; Umgiesser, G. Changes in Venice Lagoon Dynamics Due to Construction of Mobile Barriers. *Coast. Eng.* **2010**, *57*, 694–708. [[CrossRef](#)]
33. Volpe, V.; Silvestri, S.; Marani, M. Remote Sensing Retrieval of Suspended Sediment Concentration in Shallow Waters. *Remote Sens. Environ.* **2011**, *115*, 44–54. [[CrossRef](#)]
34. Carniello, L.; Silvestri, S.; Marani, M.; D’Alpaos, A.; Volpe, V.; Defina, A. Sediment Dynamics in Shallow Tidal Basins: In Situ Observations, Satellite Retrievals, and Numerical Modeling in the Venice Lagoon. *J. Geophys. Res. Earth Surf.* **2014**, *119*, 802–815. [[CrossRef](#)]
35. Braga, F.; Zaggia, L.; Bellafiore, D.; Bresciani, M.; Giardino, C.; Lorenzetti, G.; Maicu, F.; Manzo, C.; Riminucci, F.; Ravaioli, M.; et al. Mapping Turbidity Patterns in the Po River Prodeltà Using Multi-Temporal Landsat 8 Imagery. *Estuar. Coast. Shelf Sci.* **2017**, *198*, 555–567. [[CrossRef](#)]
36. Cucco, A.; Umgiesser, G. Modeling the Venice Lagoon Residence Time. *Ecol. Model.* **2006**, *193*, 34–51. [[CrossRef](#)]
37. Helsby, R. Sand Transport in Northern Venice Lagoon through the Tidal Inlet of Lido. Ph.D. Thesis, University of Southampton, Southampton, UK, 2008.
38. Cosoli, S.; Mazzoldi, A.; Gačić, M. Validation of Surface Current Measurements in the Northern Adriatic Sea from High-Frequency Radars. *J. Atmos. Ocean. Technol.* **2010**, *27*, 908–919. [[CrossRef](#)]
39. Zuliani, A.; Zaggia, L.; Collavini, F.; Zonta, R. Freshwater Discharge from the Drainage Basin to the Venice Lagoon (Italy). *Environ. Int.* **2005**, *31*, 929–938. [[CrossRef](#)]
40. Collavini, F.; Bettiol, C.; Zaggia, L.; Zonta, R. Pollutant Loads from the Drainage Basin to the Venice Lagoon (Italy). *Environ. Int.* **2005**, *31*, 939–947. [[CrossRef](#)]
41. Simpson, M.R.; Bland, R. Methods for Accurate Estimation of Net Discharge in a Tidal Channel. *IEEE J. Ocean. Eng.* **2000**, *25*, 437–445. [[CrossRef](#)]
42. Brando, V.E.; Braga, F.; Zaggia, L.; Giardino, C.; Bresciani, M.; Matta, E.; Bellafiore, D.; Ferrarin, C.; Maicu, F.; Benetazzo, A.; et al. High-Resolution Satellite Turbidity and Sea Surface Temperature Observations of River Plume Interactions during a Significant Flood Event. *Ocean Sci.* **2015**, *11*, 909–920. [[CrossRef](#)]
43. Braga, F.; Scarpa, G.M.; Brando, V.E.; Manfè, G.; Zaggia, L. COVID-19 Lockdown Measures Reveal Human Impact on Water Transparency in the Venice Lagoon. *Sci. Total Environ.* **2020**, *736*, 139612. [[CrossRef](#)]
44. Pahlevan, N.; Chittimalli, S.K.; Balasubramanian, S.V.; Vellucci, V. Sentinel-2/Landsat 8 Product Consistency and Implications for Monitoring Aquatic Systems. *Remote Sens. Environ.* **2019**, *220*, 19–29. [[CrossRef](#)]
45. Vanhellemont, Q.; Ruddick, K. Atmospheric Correction of Metre-Scale Optical Satellite Data for Inland and Coastal Water Applications. *Remote Sens. Environ.* **2018**, *216*, 586–597. [[CrossRef](#)]
46. Vanhellemont, Q. Adaptation of the Dark Spectrum Fitting Atmospheric Correction for Aquatic Applications of the Landsat and Sentinel-2 Archives. *Remote Sens. Environ.* **2019**, *225*, 175–192. [[CrossRef](#)]
47. Dogliotti, A.I.; Ruddick, K.G.; Nechad, B.; Doxaran, D.; Knaeps, E. A Single Algorithm to Retrieve Turbidity from Remotely-Sensed Data in All Coastal and Estuarine Waters. *Remote Sens. Environ.* **2015**, *156*, 157–168. [[CrossRef](#)]
48. Nechad, B.; Ruddick, K.G.; Park, Y. Calibration and validation of a generic multisensor algorithm for mapping of total suspended matter in turbid waters. *Remote Sens. Environ.* **2010**, *114*, 854–866. [[CrossRef](#)]

49. Barsi, J.A.; Barker, J.L.; Schott, J.R. An Atmospheric Correction Parameter Calculator for a Single Thermal Band Earth-Sensing Instrument. In Proceedings of the IGARSS 2003 IEEE International Geoscience and Remote Sensing Symposium (IEEE Cat. No. 03CH37477), Toulouse, France, 21–25 July 2003; Volume 5, pp. 3014–3016.
50. Braga, F.; Ciani, D.; Colella, S.; Organelli, E.; Pitarch, J.; Brando, V.E.; Bresciani, M.; Concha, J.A.; Giardino, C.; Scarpa, G.M.; et al. COVID-19 lockdown effects on a coastal marine environment: Disentangling perception versus reality. *Sci. Total Environ.* **2022**, *817*, 153002. [[CrossRef](#)] [[PubMed](#)]
51. Molinaroli, E.; Guerzoni, S.; Sarretta, A.; Masiol, M.; Pistolato, M. Thirty-Year Changes (1970 to 2000) in Bathymetry and Sediment Texture Recorded in the Lagoon of Venice Sub-Basins, Italy. *Mar. Geol.* **2009**, *258*, 115–125. [[CrossRef](#)]